

Magma decompression rate correlates with explosivity at basaltic volcanoes – Constraints from water diffusion in olivine

Anna Barth^{a,*}, Megan Newcombe^f, Terry Plank^a, Helge Gonnermann^b, Sahand Hajimirza^b, Gerardo J. Soto^c, Armando Saballos^d, Erik Hauri^e

^aLamont Doherty Earth Observatory, United States of America

^bRice University, United States of America

^cEscuela Centroamericana de Geología & Red Sismológica Nacional, Universidad de Costa Rica, Costa Rica

^dInstituto Nicaraguense De Estudios Territoriales, Nicaragua

^eCarnegie Institution of Washington, United States of America

^fUniversity of Maryland, United States of America



ARTICLE INFO

Article history:

Received 27 February 2019

Received in revised form 9 August 2019

Accepted 17 August 2019

Available online 28 August 2019

ABSTRACT

Despite the strong theoretical basis for the importance of magma decompression rate in modulating the dynamics of explosive basaltic eruptions, few measurements exist. Here, we quantify magma decompression rate using the incomplete diffusive re-equilibration of water through olivine for two contrasting eruptions at Cerro Negro volcano in Nicaragua: the 1992 VEI 3 and 1995 VEI 2 eruptions. Both eruptions have the same basaltic composition ($\text{SiO}_2 \sim 50 \text{ wt\%}$) and maximum volatile concentrations ($\text{H}_2\text{O} \sim 4.7 \text{ wt\%}$). SIMS and NanoSIMS measurements of water in olivine-hosted melt inclusions (MIs) from both eruptions show a negative correlation between MI size and water loss, as predicted for diffusive re-equilibration. MIs from the 1995 eruption appear to have experienced more water loss compared to those from the 1992 eruption (up to 80–90% water loss in MIs $< 50 \mu\text{m}$), which is consistent with slower magma ascent.

Quantifying the timescale for water diffusion during magma decompression requires an accurate constraint on H^+ diffusivity through olivine. We perform dehydration experiments on oriented cuboids of olivine from Cerro Negro in a 1 atm. furnace at 800 and 1000 °C and at an oxygen fugacity 0.25 log units above the nickel-nickel oxide buffer ($\text{NNO} + 0.25$) in a sequence of heating steps. Between each heating step we measure the H^+ concentration along each crystallographic direction by FTIR and model these profiles to determine the diffusivity. We find the fastest diffusion direction along a_{\parallel} and develop an Arrhenius relationship for the diffusivity along this direction: $D_a(\text{m}^2/\text{s}) = 9.6 \times 10^{-6} \exp\left(\frac{-125}{RT}\right)$, where R is the gas constant 8.314 J/mol K; T is the temperature in K and the activation energy is 125 kJ/mol. These are the fastest rates ever measured for olivine dehydration, which may relate to the low forsterite content of the olivines ($\text{Fo} \sim 79$).

We have developed a 1D model for H^+ diffusion along the fast direction since this dominates water loss ($D_a > 10 \times D_b$ or D_c). Using our new H^+ diffusivity, we model water diffusion from MIs during magma decompression to determine ascent timescales. We find that magma from the VEI 3 eruption of 1992 ascended at a median rate of 0.007 MPa/s, which is $\sim 5 \times$ faster than the median for the 1995 VEI 2 eruption, although both eruptions show a \sim two orders of magnitude spread in decompression rate. Assuming linear decompression, this places a minimum bound of $\sim 6.5 \text{ h}$ on magma ascent during the 1992 eruption and $\sim 35 \text{ h}$ for the 1995 eruption. Monte Carlo simulations give a 2σ uncertainty on $\log_{10}(dP/dt)$ of $\sim 10\%$ – much smaller than the order of magnitude spread in decompression rate within each eruption, which suggests that there is real variation in decompression rate for a given deposit. Our results support the hypothesis that higher decompression rates are correlated with more explosive eruptions and show that diffusion modelling of MI water loss is a powerful tool that is sensitive to changes in decompression between VEI 2 and 3 eruption intensities.

© 2019 Published by Elsevier B.V.

* Corresponding author.

E-mail address: abarth@ldeo.columbia.edu (A. Barth).

1. Introduction

Volcanic eruptions are driven by processes occurring in the conduit as magma ascends towards the surface. Chief among these is the depressurization-induced volatile exsolution which rapidly increases the magma's buoyancy. The extent to which the bubbles are able to segregate from the melt controls the ability of the magma to fragment and erupt explosively (Gonnermann and Manga, 2007). Other processes, such as crystallization and shear heating at the conduit margins further modulate the eruptive style through their control on magma viscosity (Costa et al., 2007). All of these processes have feedbacks with ascent rate. This is the basis for the suggestion that ascent rate may influence the style of eruption (Cashman, 2004; Edmonds, 2008; Gonnermann and Manga, 2013; Wilson and Head, 1981).

Initial dissolved volatile contents have often been cited as a controlling factor for the style of eruption (e.g. Andújar and Scaillet, 2012). For example, the transition from explosive to effusive styles during an eruption has been previously attributed to progressively tapping deeper portions of a magma chamber that is stratified in its volatile concentrations (e.g. Eichelberger and Westrich, 2012). However, as pointed out in a recent review by Cassidy et al. (2018), the dissolved volatiles in melt inclusions (MIs) rarely support this claim, with no correlation between maximum dissolved volatile contents and explosivity. Instead, the effect of volatiles on eruption style seems more likely to arise from the rate of bubble exsolution and style of degassing (i.e. closed versus open), which are both controlled by the magma decompression rate.

Despite its clear importance in eruption dynamics, few estimates of ascent or decompression rate exist, especially for hydrous basaltic to intermediate magmas. Those that have been made often yield contradictory results, depending on the method used. In particular, laboratory experiments involving crystallization or reaction rims typically yield slower decompression rates, while vesiculation experiments give much faster rates, and have been suggested to reflect the highly-accelerated final stages of ascent and not the integrated decompression path (e.g. Geschwind and Rutherford, 1995; Taramaru, 2006; Humphreys et al., 2008; Cassidy et al., 2018 – their Fig. 5).

In order to isolate the effects of decompression rate on eruption style, we determine decompression rates for two eruptions at the same volcano – Cerro Negro in Nicaragua. The 1992 VEI 3 eruption produced a 7 km high ash cloud, whereas the subsequent 1995 VEI 2 eruption was dominated by fire fountaining and concurrent lava flows (Hill et al., 1998; Roggensack et al., 1997). Roggensack et al. (1997) saw differences in the volatile systematics for the 1992 and 1995 magma and proposed that there could be a difference in ascent rate for the different eruptions. Our work aims to test this hypothesis.

Magma composition is similar for the two eruptions (basaltic with 50 wt % SiO₂), including crystal content, so viscosity should be similar for the two magmas (Hill et al., 1998, our Supplementary Data). Furthermore, it is thought that conduit geometry was similar for the two eruptions because Cerro Negro's cone morphology was the same for the two eruptions and the vent location has been stable for ~150 years (Roggensack et al., 1997). Thus, the 1992 and 1995 eruptions at Cerro Negro present an ideal opportunity to test the hypothesis that decompression rate is a controlling factor in determining the style of eruption at basaltic to intermediate volcanoes.

1.1. Approach

As magma ascends, volatile solubility decreases and the melt loses its volatiles to bubbles. Melt inclusions (MIs) within crystals carried with this ascending magma will begin to diffusively lose water to the surrounding melt. However, depending on the timescale

of ascent, H⁺ diffusion through olivine may be too slow for the MIs to remain in equilibrium with the degassing magma, allowing olivine-hosted MIs to preserve a higher water concentration than the host magma. We can exploit this disequilibrium and use diffusion modelling of H⁺ in olivine to constrain magma decompression rates.

We have developed a diffusion model of H⁺ diffusion from MIs through their host olivine into surrounding degassing melt, which is modelled as a specified concentration boundary condition. This is similar to previous models which assumed a spherical MI at the centre of a spherical olivine with isotropic diffusion (Chen et al., 2013; Gaetani et al., 2012; Ni et al., 2017; Qin et al., 1992). However, given the strongly anisotropic nature of H⁺ diffusivity in olivine (Kohlstedt and Mackwell, 1998; Le Voyer et al., 2014; Ferriss et al., 2018; this study), we model 1D diffusion along the fast **a**_ direction of the host olivine (note that we will use **a**_, **b**_, **c** _ from now on to denote crystallographic directions along [100], [010], and [001], respectively). Although this is an approximation, Thoraval and Demouchy (2014) showed that this is justified as long as the 1D profile is modelled along the fast direction, and that the diffusion coefficient along that direction is at least ten times faster than the two slower crystallographic directions. Under these conditions, the results from a 1D model are indistinguishable from those of a full 3D anisotropic model (Thoraval and Demouchy, 2014 – their Fig. 3).

MIs lose water through the olivine at a rate dependent on the diffusivity of water through olivine, D_H, the partition coefficient between melt and olivine, k_D, the MI size, and distance between the MI and the olivine rim (Chen et al., 2013; Qin et al., 1992). Small inclusions lose water more rapidly than large inclusions due to their higher surface area to volume ratio and lower mass of water. Estimating the initial water concentration of the MIs using systematics of incompatible elements, such as K₂O, allows us to estimate the amount of water lost from the MI by diffusion (Lloyd et al., 2013).

One of the main difficulties with water-in-olivine diffusion modelling is the orders of magnitude variation in diffusivity estimates (Chen et al., 2011; Ferriss et al., 2018; Kohlstedt and Mackwell, 1998; Padrón-Navarta et al., 2014). Some of this variation is due to effects of anisotropic diffusion, while the rest is likely due to a range in olivine composition, particularly Fe content. H⁺ diffusion in pure forsterite has been measured to be several orders of magnitude slower than Fe-bearing olivines from Kilauea and San Carlos (Fo~90) (Ferriss et al., 2018). This dependence of H⁺ diffusivity on Fe content has also been found in clinopyroxene (Ferriss et al., 2016) and indicates the importance of Fe for the redox reactions necessary for the fast 'proton-polaron' diffusion mechanism. In order to determine water diffusivities appropriate to the system we are studying, we performed dehydration experiments on oriented olivine phenocrysts from Cerro Negro.

2. Background - H⁺ diffusivity

Water is dissolved in melt inclusions as H₂O and OH⁻ and can re-equilibrate with surrounding melt by transport of H⁺ ions through the olivine lattice. While in the olivine lattice, water exists as H⁺ bonded to structural oxygen in point defects. We therefore will refer to water as H⁺ when discussing its diffusion through olivine. The amount of H⁺ hosted by different defects can be distinguished by differences in wavelength of absorption bands measured by Fourier-Transform Infrared Spectroscopy (FTIR) (Beran, 1969; Berry et al., 2005). In this paper, we do not focus on differences between defects because bulk H⁺ diffusion is most relevant for MI re-equilibration.

There are two principal experimental methods to determine diffusivity from dehydration experiments. The first is based on changes in concentration at a particular position within the crystal over time, while the second is based on changes in concentration with distance across the crystal at a given time. The first method will be referred

to as the thin-slab approach and involves a point measurement at the centre of a slab, assuming that water loss is confined to the direction normal to the slab plane. The second is the whole-block method (Ferriss et al., 2015) and measures concentration profiles along each crystallographic direction to determine the diffusivity along each direction. The thin-slab method is easier in terms of sample preparation and data collection because it requires the crystal to be polished into a slab instead of a cuboid and uses one data point instead of a whole profile. However, the thin-slab method only provides an estimate of diffusivity in the direction normal to the slab plane, whereas the whole-block method constrains diffusivity along all three crystallographic directions. Moreover, the diffusion timescale can be estimated with more precision by using multiple points along a profile rather than a single point measurement.

2.1. Thin-slab

The thin-slab method is based on the solution of Fick's second law for one-dimensional diffusion in a solid with an homogeneous initial concentration bounded by two parallel planes (Fig. 1), in this case \mathbf{a}_\perp planes. During diffusive re-equilibration, the concentration profile that develops along \mathbf{a}_\perp after time, t , may be described by

$$C(x, t) = \frac{4C_0}{\pi} \sum_{n=0}^{\infty} \frac{(-1)^n}{2n+1} \exp\left(-\frac{Dt(2n+1)^2\pi^2}{4L^2}\right) \cos \frac{(2n+1)\pi x}{2L} \quad (1)$$

where C_0 is the initial (homogeneous) H^+ concentration, D is the diffusion coefficient of H^+ along \mathbf{a}_\perp , and L is the half thickness of the sample (Crank, 1975).

The FTIR measurement in the centre of this slab reflects the average concentration along this profile, which is given by

$$C_{av} = \frac{8C_0}{\pi^2} \sum_{n=0}^{\infty} \frac{1}{(2n+1)^2} \exp\left(-\frac{Dt(2n+1)^2\pi^2}{4L^2}\right) \quad (2)$$

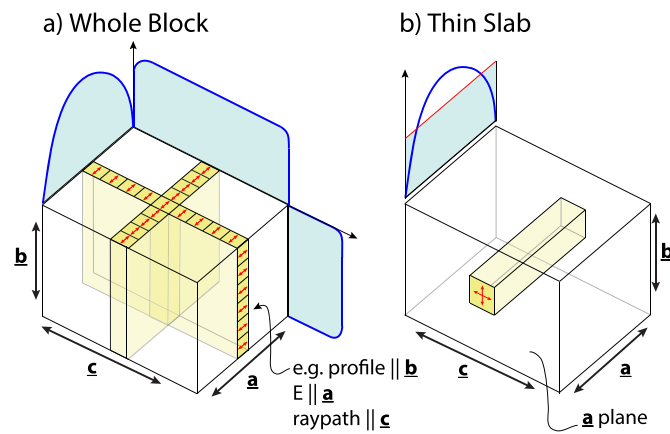


Fig. 1. Schematic diagram showing position and polarisation of measurements for whole-block and thin-slab methods. Yellow volume shows region probed by IR radiation – each square on olive block surface shows position of point measurement along profile. Red arrows show IR polarisation direction for each measurement. Blue lines show approximate shape of diffusion profile along each crystallographic direction. Thin-slab method does not consider these profiles but only the average water concentration (red line) along the ray path. Note that for the thin-slab method to be valid, the slab thickness along the ray path (in this case \mathbf{a}_\perp) need only be thin enough such that diffusion reaches the centre of the crystal along only this direction. Since D_a is so much faster than D_b or D_c , this can be achieved even in a cubic geometry. (For interpretation of the references to color in this figure legend, the reader is referred to the web version of this article.)

The diffusivity along \mathbf{a}_\perp may be calculated by fitting the solution to this equation to the variation of C_{av}/C_0 over time, where C_{av}/C_0 is determined from the FTIR measurements and time is the duration of the heating experiments.

2.2. Whole-block

The whole-block method was developed by Ferriss et al. (2015) and provides a way to use concentration profiles (absorption profiles from FTIR) measured in all three crystallographic directions to determine 3D diffusivity. The method is based on a forward 3D diffusion model that takes into account the fact that each FTIR measurement is averaged along a ray path that is zoned in water (Fig. 1). Each measurement provides a data point for the profile that it is part of, but also adds a constraint to the perpendicular profile along the IR ray path. Further details of this method can be found in Ferriss et al. (2015).

3. Eruption description and samples

We focussed on the 1992 VEI 3 and 1995 VEI 2 eruptions of Cerro Negro. The 1992 eruption was purely explosive and produced a sustained 7 km high ash cloud. The eruption lasted 3.6 days (April 9–13) and produced a tephra volume of 0.011 km^3 (dense-rock equivalent, DRE). By contrast, the 1995 eruption had a 2–3 km high ash plume and 80% of the erupted material was lava. The eruption lasted for 13 days (November 19 to December 2nd), although appreciable tephra deposits only formed in the last 4 days. The eruption produced 0.0013 km^3 (DRE) of tephra and 0.0037 km^3 (DRE) of lava, or about half the total volume emitted in 1992.

In terms of chemistry and petrography, the 1995 eruption is remarkably uniform throughout the lava and fall deposits (Hill et al., 1998). This is in contrast to the 1992 eruption, which is zoned in whole rock composition due to variations in crystal proportions – the upper part of the fall section has almost twice the olivine and augite as the base (Hill et al., 1998). Our major and trace element data support previous work (Hill et al., 1998; Walker and Carr, 1986) showing that the bulk rock compositions for the two eruptions have virtually identical trace element concentrations, including rare-earth element patterns (see Supplementary Data). Furthermore, the olivine populations from the two eruptions have the same range in forsterite content (71.5–82). The consistency of magma composition over the course of many eruptions suggests the presence of a stable magma reservoir at depth (Venugopal et al., 2016).

Samples consist of ash and lapilli from the 1992 and 1995 eruptions (Fig. 2). The 1992 samples were collected by Gerardo Soto and provided by Mike Carr, and consist of a distal ash sample collected April 14th from the town of Leon, 22 km SW of Cerro Negro, and a proximal ash and lapilli sample collected April 13th, 0.5 km NW of the crater (IGSN: IEACB0004, IEACB0005 – see Supplementary Data for URL).

During the 1992 eruption, the explosive paroxysm started on April 9 at 23:45 and lasted until 16:05 on April 12 (McClelland, 1992). Less steady, pulsatory activity continued until midnight on April 12. Eruption reports say that ash began to fall in León 1 h after the onset of the eruption until 17:00 on April 10, when it reached 4 cm-thick. After this, the winds changed and ash fall ceased in León. Therefore, our distal sample most likely represents the early peak of the paroxysm on April 10. The proximal sample was collected on the morning of April 13, on Cerro La Mula, where the fall deposit was >1 m thick. Material was collected from the uppermost portion of the section, and therefore derives mostly from the late paroxysmal activity.

The 1995 samples were collected by the authors Anna Barth and Armando Saballos during field work in August 2016 (IGSN: IEACB0003). A 1.5 m deep trench was dug at the western edge of the cone at the slope break (Fig. 2b). The 1995 sample comes from

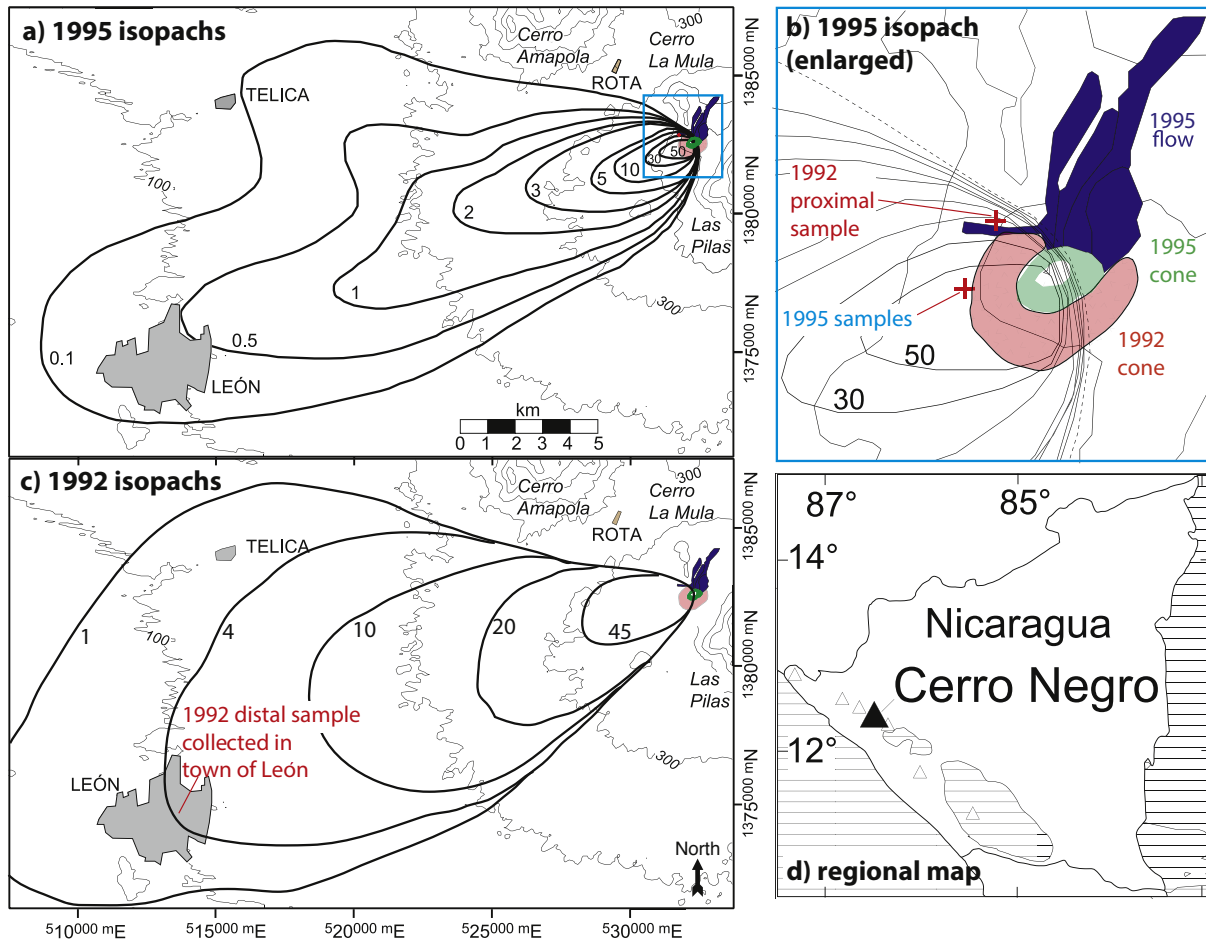


Fig. 2. (a) Map modified from Hill et al. (1998) showing sample locations. Contours are isopachs for 1995 tephra-fallout in cm. Location of enlarged section (b) shown by blue square in (a). (b) 1995 lava flow and cone shown in colour. (c) 1992 isopach map from McClelland (1992). Note the difference of scale between 1992 and 1995 isopachs. (d) shows location of major Nicaraguan volcanoes. (For interpretation of the references to color in this figure legend, the reader is referred to the web version of this article.)

the top 15 cm; below this we encountered coarser material with high MgO (~8 wt%—Supplementary Data), consistent with the final magma erupted in 1992 (Hill et al., 1998). Within the 1995 deposit, there appeared to be fine scale layering, defined by slight changes in grain size and so three 5 cm layers were sampled separately (see IGSN: IEACB0003).

4. Methods

4.1. Dehydration experiments

4.1.1. Starting material

Two Cerro Negro olivines were oriented and polished into cuboids of sizes $1087 \times 405 \times 922$ and $577 \times 944 \times 1073 \mu\text{m}$ along \mathbf{a}_\perp , \mathbf{b}_\perp , and \mathbf{c}_\perp (CN-block 1 and CN-block 2, respectively). Sample thicknesses in all three crystallographic directions were measured with a digital micrometer accurate to within $\pm 5 \mu\text{m}$. Crystallographic directions were determined from crystal morphology (Supplement) and confirmed with electron backscatter diffraction (EBSD).

The original rims contained low water concentrations and were polished off, resulting in homogeneous profiles within analytical uncertainty (10%). Major and trace element concentration profiles measured by laser ablation inductively coupled plasma mass spectrometry (LA ICP-MS) revealed minimal zoning in major elements, including forsterite which varied from 77.9 to 80.2% (Supplementary

Data). We did, however, find significant zoning in some minor elements (Al, Cr, Ni), although we do not believe that this has played a significant role in H^+ diffusion given the flat initial water profiles (Fig. 5).

4.1.2. Defect structure of starting material

We observe several absorption peaks in the O-H stretching region of $3150\text{--}3600 \text{ cm}^{-1}$ of the olivine FTIR spectra (Fig. 3). The largest peaks are seen with the electric vector polarised parallel to \mathbf{a}_\perp ($E \parallel \mathbf{a}_\perp$). Following Padrón-Navarta et al. (2014) and Ferriss et al. (2018), the peaks at 3328 , 3358 cm^{-1} are a doublet associated with a Mg^{2+} vacancy charge-balanced by H^+ and trivalent ion (Fe^{3+} , Cr^{3+} , Al^{3+}) substituting on a metal site, [Triv]; the peaks at 3524 and 3572 cm^{-1} are a doublet created by 2 H^+ coupled with Si^{4+} vacancy and Ti^{4+} on a metal site [Ti] (Fig. 3).

4.1.3. Dehydration experiments

Both olivine blocks were heated for two 20 minute increments using a vertical furnace as described in Ferriss et al. (2015), with oxygen fugacity controlled by $\text{CO}\text{-}\text{CO}_2$ gas mixing at $\text{NNO} + 0.25$ based on Fe-S systematics in Cerro Negro MIs determined by Portnyagin et al. (2014). CN-block 1 was heated at 1000°C and an oxygen fugacity of $10^{-10.08}$ bars, while CN-block 2 was heated at 800°C and an oxygen fugacity of $10^{-13.65}$ bars (Table 1).

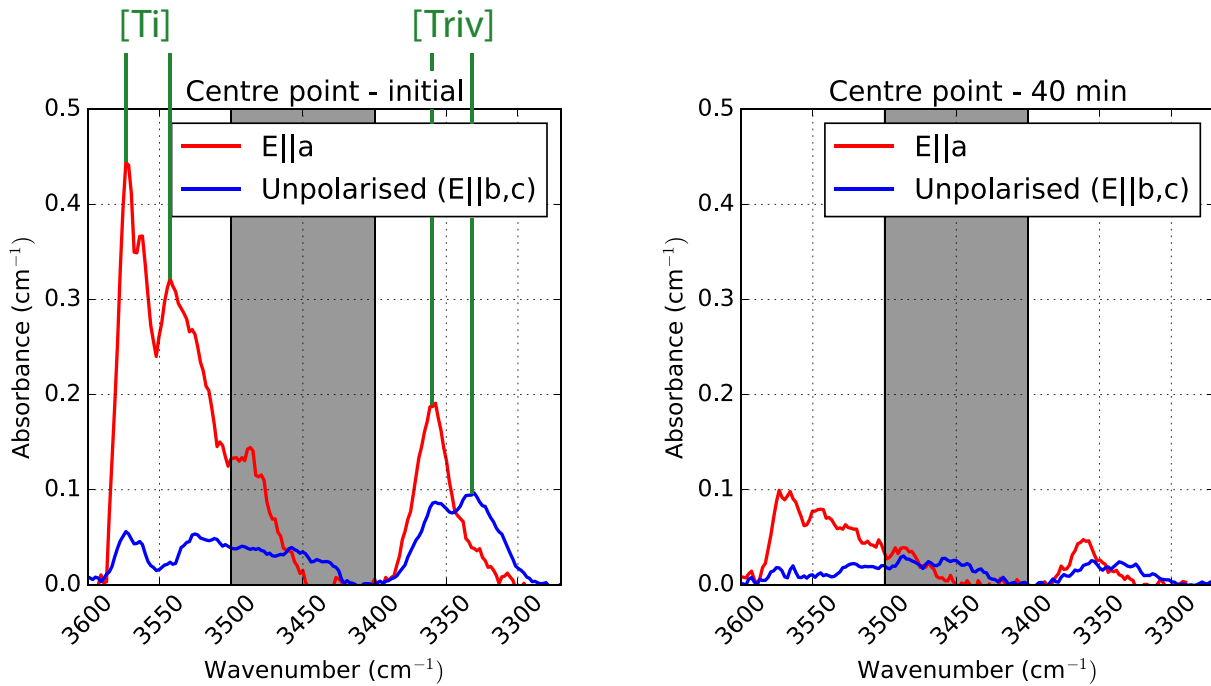


Fig. 3. CN block 1 spectra taken through the centre of the crystal before heating (left) and after 40 min of heating at 1000 °C (right). Measurements with $E \parallel a$ (red) used in whole-block method, unpolarised measurements (blue) used for thin-slab method. Most water is held in [Ti] and [Triv] defects (green labels) although we do not model these separately since MI re-equilibration, the focus of this study, reflects bulk H⁺ diffusion. For whole-block method, entire area under the curve from wavenumber 3150–3600 cm⁻¹ is summed for bulk water. For thin-slab method, we sum area under curve excluding mid-wavenumber region (grey; 3400–3500 cm⁻¹). See text for further details. (For interpretation of the references to color in this figure legend, the reader is referred to the web version of this article.)

We monitored temperature using an S-type thermocouple, and oxygen fugacity with a zirconia sensor. The sample was kept at the top of the furnace until both temperature and fo_2 equilibrated, and was then lowered into the hot spot next to the thermocouple.

4.1.4. Determination of hydrogen in experimental olivine blocks

The hydrogen (H⁺) concentration was measured in the experimental olivine blocks before and after each heating step. Spectra were collected using the Thermo Nicolet Nexus 670 infrared spectrometer and Thermo Nicolet Continuum 15× infrared microscope at the American Museum of Natural History, with an aperture of 100 × 100 μm, a resolution of 4 cm⁻¹, and averaged over 200 scans. Where higher spatial resolution was required, the aperture was reduced to 50 × 100 μm and the number of scans increased to 300. Some measurements were taken multiple times with different apertures, and the resulting peak areas were found to be within 5% of each other.

We fit a quadratic baseline through the spectra between wavenumbers 3150 and 3600 cm⁻¹ and forced the baseline through the spectra at 3400 cm⁻¹ (Fig. 3). This is to provide consistency among measurements along the profile, before and after the experiment (e.g., Ingrin et al., 1995). Profiles for the whole-block method

were measured with a ZnSe polariser parallel to a . Measurements for the thin-slab method were taken with the ray path along a and therefore could not be polarised parallel to a . For CN-block 1 we took unpolarised measurements, for CN-block 2 we averaged measurements with $E \parallel b$ and $E \parallel c$. We estimate total absorbance by integrating the total area between the baseline and absorbance spectrum. We focus on the [Ti] and [Triv] peaks since these are the best expressed for all polarisation directions, and so exclude the region 3400–3500 cm⁻¹ from our area integration (Fig. 3).

Using the Bell calibration we estimate initial water concentrations for CN-block 1 and CN-block 2 to be ~9 and 5 ppm, respectively, (~6 and 3 ppm using the Withers calibration) (Bell et al., 2003; Withers et al., 2012). These are necessarily estimates because we did not take measurements with the polariser along each crystallographic direction (further discussion in Supplement). However, the diffusivity is insensitive to absolute water concentrations since all concentrations are normalised by the initial concentration.

4.2. Melt inclusion chemistry

4.2.1. Melt inclusion preparation

Seventy-six MI-bearing olivines were mounted individually in dental resin and polished to the maximum width of the MI using diamond pads down to a grit size of 0.25 μm. A range of MI sizes were chosen in order to capture the relationship between diffusive water loss and MI size. In particular, we focused on measuring small (<30 μm) MIs, which was made possible using NanoSIMS, as these should undergo greater extents of re-equilibration. We then cleaned the samples in ultrasonic baths of toluene, acetone and isopropanol, baked them in a vacuum oven at 110 °C for several days and pressed the crystals into indium mounts. Olivine orientation was determined by crystal morphology (Supplement). All measured MIs are glassy with a single shrinkage bubble and no crystals. Only crystals which

Table 1
Experimental run conditions.

	CN block 1	CN block 2
Size (μm)	1087 × 405 × 922	577 × 944 × 1073
Temp (°C)	1000	800
Time (min)	20, 40	20, 40
NNO	+0.25	+0.25
log fo_2 (bars)	-10.08	-13.65
Analytical treatment	Whole-block and thin-slab	Thin-slab

Experimental conditions and bulk H⁺ diffusivity results for dehydration experiments.

had the \mathbf{a}_\perp direction exposed in the polished plane were selected for diffusion modelling (8 for 1992, 35 for 1995) because water loss along \mathbf{a}_\perp dominates diffusion (see below) and therefore the distance between the MI and olivine edge along \mathbf{a}_\perp is an important parameter to constrain.

4.2.2. SIMS and NanoSIMS

Volatiles (H_2O , CO_2 , Cl, F, and S) and P in the MIs and olivines were measured on a Cameca IMS 6f ion probe (SIMS) at the Carnegie Institute of Washington (CIW), Department of Terrestrial Magnetism. Small MIs ($<30\text{ }\mu\text{m}$ diameter) were measured using the Cameca NanoSIMS 50L. The indium mounts were gold-coated and placed into the sample exchange chamber one to three days before the start of the session. To remove the gold coat and any surface contamination we pre-sputtered for 120 s before beginning the data collection.

Analytical procedures followed those of Hauri et al. (2002), using a basaltic glass calibration curve, and in all cases measuring H_2O as $^{16}\text{O}^1\text{H}$ and CO_2 as ^{12}C . A primary beam of Cs ions (5–10 nA) accelerated to 10 kV was used to create a 20–40 μm spot size. $^{30}\text{Si}^-$ was used as a denominator for all reported ion intensity ratios. Within each session, replicate analyses of basaltic andesite standard glass MR:ND-70-01 (Lloyd et al., 2013) yielded relative standard deviations (100 * standard deviation/mean) of <4.6% for CO_2 , <5.4% for H_2O , <4.8% for F, <10% for S, and <19% for Cl.

4.2.3. Electron microprobe

MIs and olivines were analysed for major elements using a Cameca SX100 microprobe (EMP) at the AMNH. MI analyses were performed as close to the centre of the inclusion as possible. The host olivine was analysed at $\sim 20\text{ }\mu\text{m}$ from the border with the inclusion.

During all sessions, major elements in hydrous glasses and olivine phenocrysts were analysed using a 10-nA beam current (4-nA for Na) and a 15-kV accelerating potential with a 12 μm diameter beam. Count times for major elements were 30 s on peak and 15 s for backgrounds. Na_2O was counted for 2 s on peak and 20 s on background; FeO^T count times were 20 s on peak and 15 s for background; Sulfur was measured on the sulfate peak position and was standardized on BaSO_4 .

Replicate analysis of four basaltic glass check standards FR:ND-60-01 yielded an average relative standard deviation of <2.5% for K_2O and <10% for the remainder of the major elements. To correct for inter-run calibration offsets, all analyses were corrected using factors determined from the accepted values for the FR:ND-60-01 check standard (see Supplementary Data, values from Lloyd et al., 2013).

4.2.4. Correction for post-entrapment modification

To know the concentration of elements in the melt at the time of MI entrapment, a correction needs to be made for post-entrapment crystallization (PEC), which occurs during cooling or MI water loss (Danyushevsky et al., 2000; Steele-Macinnis et al., 2011). We correct for PEC by adding equilibrium olivine into the MI composition, in incremental fractions of 0.25 wt %, until it is in equilibrium with its host olivine. The amount of PEC calculated for the MIs ranges from 0 to 9 wt %. There are two variables used in calculating the equilibrium olivine composition: the K_D value and the $\text{Fe}^{3+}/\text{Fe}_T$ ratio. We calculate a K_D of 0.35 using the formulation in Toplis (2005). For $\text{Fe}^{3+}/\text{Fe}_T$, we use a value of 0.2 based on an f_{O_2} of NNO + 0.25 for Cerro Negro (Portnyagin et al., 2014) and the relationship between f_{O_2} and $\text{Fe}^{3+}/\text{Fe}_T$ from Kress and Carmichael (1991).

We determine the entrapment temperature for each MI using olivine-liquid thermometry based on Eq. 4 in Putirka et al. (2007) and no difference in temperature was found between the two eruptions. 1100°C is the average temperature calculated, with a full range of 1076 – 1130°C and standard deviation of 12°C .

5. Results

5.1. Diffusivity of water in olivine

Diffusivity was determined by the thin-slab method for both blocks at 800 and 1000°C and was compared with results from the whole-block method for CN-block 1 at 1000°C . Fig. 4 shows C_{av}/C_0 over time for the blocks heated at 800 and 1000°C with curves representing analytical solutions to Eq. (2). Within our estimated error based on baseline choice (see Supplement), H^+ diffusivity is constant over the course of the experiments: $10^{-11.1}\text{ m}^2/\text{s}$ at 800°C and $10^{-10.14}\text{ m}^2/\text{s}$ at 1000°C .

The whole-block method gives the same diffusivity as the thin-slab method for CN-block 1 at 1000°C along \mathbf{a}_\perp ($D_a = 10^{-10.14}\text{ m}^2/\text{s}$). Fig. 5 shows H^+ profiles measured along each crystallographic direction for bulk water (i.e. total area between spectra and baseline). OH^- absorption areas for each profile are normalised to the average area measured along that profile for the initial, undehydrated olivine. The agreement of the whole-block and thin-slab method at 1000°C gives us confidence in our results, and suggests that the less data-intensive thin-slab method is sufficient, as long as the sample is analysed along the axis of most rapid diffusion (in this case, the olivine \mathbf{a}_\perp -axis).

Curves in Fig. 5 show best-fit whole-block model predictions for 20 and 40 min. Some uncertainty arises because of the choice of H^+ concentration at the edge, which does not appear to be zero, especially for the profile after 20 min. The higher the edge concentration imposed as a boundary condition in the model, the slower the diffusivity that reproduces observed concentrations in the crystal centre. The edge concentration is varied to give the upper and lower bounds of D_a as $10^{-10.08}$ – $10^{-10.2}\text{ m}^2/\text{s}$. The fits for these bounds can be found in the Supplement.

The flat profiles along \mathbf{b}_\perp and \mathbf{c}_\perp make it impossible to accurately constrain diffusivity along these directions, but do give upper bounds on diffusivity. These are $10^{-12.5}\text{ m}^2/\text{s}$ and $10^{-11.7}\text{ m}^2/\text{s}$, along \mathbf{b}_\perp and \mathbf{c}_\perp respectively. Thus, diffusion along \mathbf{a}_\perp is $>10\times$ faster than along \mathbf{b}_\perp or \mathbf{c}_\perp .

To estimate D_H at the relevant temperatures for magma ascent at Cerro Negro, we construct an Arrhenius relationship, and extrapolate to 1100°C , which is the average temperature for both Cerro Negro eruptions based on olivine-liquid thermometry (Section 4.2.4). Fig. 6 shows our Arrhenius relationship together with diffusivity estimates from the literature. We calculate two Arrhenius relationships based on the upper and lower bounds of our measurements at 800°C

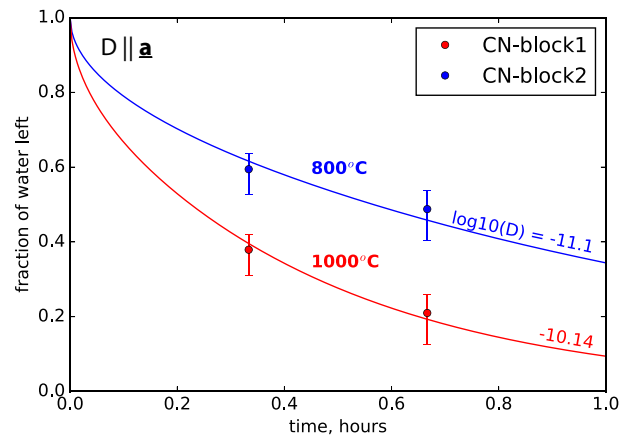


Fig. 4. Thin-slab method for CN blocks 1 and 2. C_{av}/C_0 over time for 800 and 1000°C . Fraction of water left is given by C_{av}/C_0 , where both concentrations are given by the area under the absorption curve between 3150 and 3600 cm^{-1} excluding 3400 – 3500 cm^{-1} . Curves show analytical solutions to Eq. (2). Error bars determined by varying baseline curvature (Supplement).

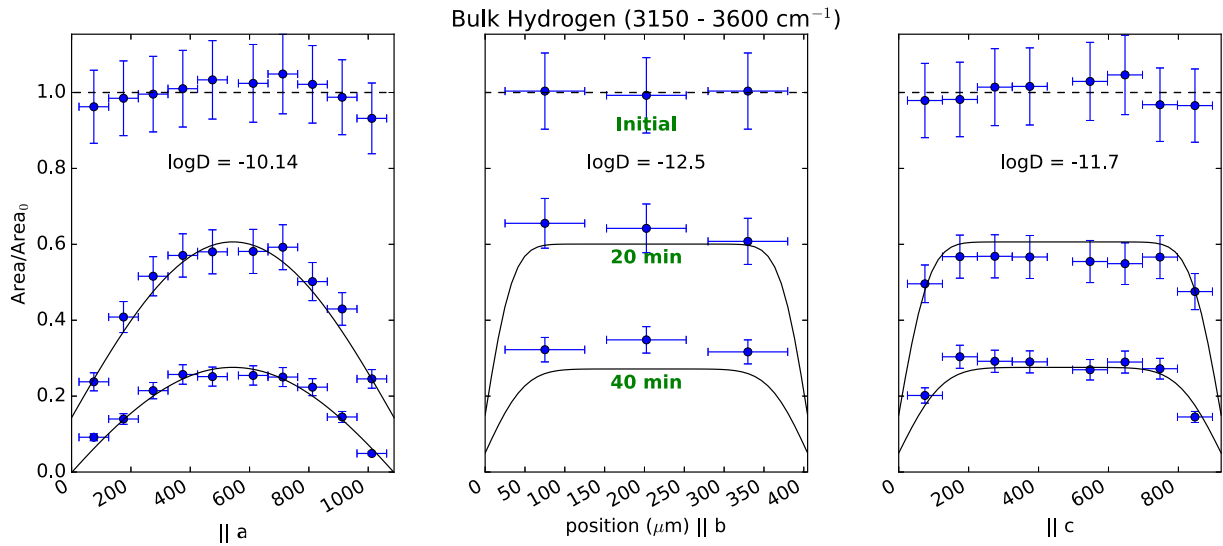


Fig. 5. Whole-block method for CN block 1 at 1000 °C. Path-integrated profiles along **a**, **b**, and **c** for bulk water (total area between 3150 and 3600 cm^{-1}). Diffusion along **a** is $>10 \times$ faster than **b** or **c**. Diffusivity estimate for **b** and **c** is an upper bound because of the flatness of the profile. The same diffusivity can be used to fit profiles after 20 and 40 min of heating.

and 1000 °C, which gives the range of D_H at 1100 °C to be $10^{-9.87}$ to $10^{-9.67} \text{ m}^2/\text{s}$. As will be discussed in Section 6.1.1, there is additional uncertainty in the diffusivity from uncertainty in magmatic temperature, which is shown by the red shaded region in Fig. 6.

5.1.1. Importance of F_e

Although the focus of this paper is the application of H^+ diffusivity for decompression rate and not the diffusion mechanism itself, it is worth discussing our rates in the context of the existing literature on H^+ diffusivity in olivine (Costa and Chakraborty, 2008; Demouchy and Mackwell, 2006; Ferriss et al., 2018; Kohlstedt and Mackwell, 1998; Padrón-Navarta et al., 2014; Peslier et al., 2015). We determined the fastest H^+ diffusivity for dehydrating olivine (Fig. 6), although faster rates have been observed during olivine hydration (proton-polaron mechanism, Kohlstedt and Mackwell, 1998). Our diffusivity is about four orders of magnitude faster than experiments on Fe-free, synthetic olivine (Padrón-Navarta et al., 2014); about two orders of magnitude faster than the ‘proton-vacancy’ mechanism (Kohlstedt and Mackwell, 1998); and also significantly faster than recent experiments on natural, Fe-bearing olivines from San Carlos and Kilauea (Fo 86–90 %) (Ferriss et al., 2018). The rapid H^+ diffusivity in our experiments is likely related to the low forsterite content of our olivines ($Fo = 79\text{--}81\%$), given that Fe is expected to play a major role in facilitating electron exchange between defects (Kohlstedt and Mackwell, 1998). The rates that we observe are too fast to involve diffusion of metal vacancies which suggests that the main diffusion mechanism at work involves the ‘proton-polaron’ mechanism – a flux of H^+ charge-balanced by a flux of electrons from Fe^{2+} to Fe^{3+} . This is consistent with the observation that the fast diffusion direction is **a** and not **c**, as would be predicted for vacancy diffusion (Le Voyer et al., 2014). Thus, increasing the iron content of olivine may enhance H^+ diffusion. A dependence of H^+ diffusivity on mineral composition highlights the benefit of measuring diffusivity in the olivine samples being studied, at least until the compositional dependence is better understood.

5.2. Melt inclusions

5.2.1. Melt inclusion chemical composition

We find overlapping melt inclusion chemistry for the three 1995 sample layers (Fig. 7). The exception is that the uppermost layer

(**A**) has lower water concentration, but this unit contains smaller MI (analysed by nanoSIMS). We attribute these lower water contents to the effect of inclusion size on diffusive water loss (see Section 5.2.2).

The two 1992 samples have overlapping H_2O concentrations but the distal sample from the early-paroxysmal phase appears to be more evolved, with higher SiO_2 , K_2O , Na_2O , and lower MgO , CaO , Al_2O_3 . The distal sample also has lower SO_2 , suggesting derivation from a shallower source.

5.2.2. Water loss from melt inclusions

Diffusion modelling of water loss from melt inclusions requires an assumption about the initial water concentrations in the inclusions at the time of entrapment. One approach is to use the maximum water concentration in a suite of MIs, implying that all MIs began with this same water concentration. However, some MIs may have been trapped after some degassing had already taken place, and so this approach would overestimate initial MI water concentrations. We correct MIs for pre-entrapment magma degassing using the coupled trends of K_2O and H_2O (Lloyd et al., 2013). Magmatic degassing is accompanied by crystallization due to the effect of water loss on the magma liquidus, which will raise the concentration of incompatible elements (e.g. K_2O) in the melt. Thus, as water decreases, K_2O increases. The 1992 and 1995 magmas have similar maximum H_2O concentrations (~4.7 wt %) and similar range of K_2O concentrations (0.2–0.8 wt%), and so we model them with a single degassing-driven crystallization curve. If this is correct and the two magmas had similar initial volatile concentrations, an interesting corollary is that initial volatile concentrations were relatively unimportant in setting the eruption style.

We model this systematic trend using Petrolog3 (Danyushevsky and Plechov, 2011) for a starting composition of 0.23 wt% K_2O , 4.7 wt% H_2O , initial and final pressures of 3 kbar and 0.85 kbar, and decompression at 30 bars/°C. Initial pressure is based on Solex modelling of CO_2 and H_2O MI concentrations, and lies within values previously reported for Cerro Negro (Portnyagin et al., 2014; Venugopal et al., 2016). While the details of the melt evolution path may change with different model parameters, the slope of the K_2O - H_2O evolution while the melt is saturated in Ol, CPx and Plag is robust to changes in initial pressure and cooling rate in Petrolog3 and MELTs.

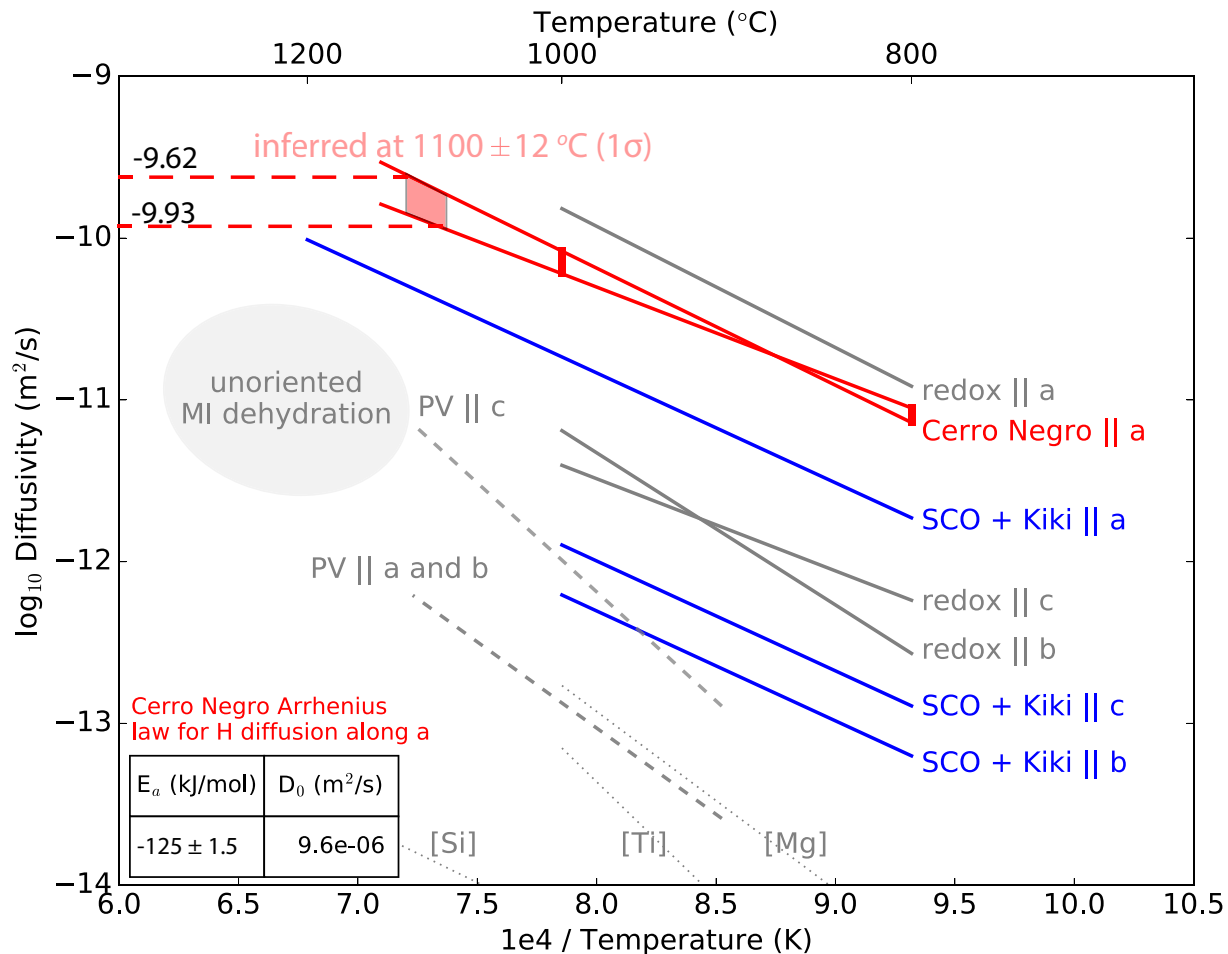


Fig. 6. Arrhenius diagram for bulk H^+ diffusion in olivine. Our diffusivity for Cerro Negro is shown in red. Vertical red bars show uncertainty from fitting procedure. Red shading shows extrapolated diffusivity at relevant temperatures with uncertainty from temperature estimate and fitting procedure. 1σ uncertainty in temperature = $12^\circ C$. Black lines show ranges for previous measurements of proton-polaron rate (redox) and proton-vacancy rate (PV) during hydratation of San Carlos olivine as well as peak-specific measurements from dehydration of synthetic forsterite (dotted lines, Padrón-Navarta et al., 2014). Blue lines show measurements on San Carlos and Kilauea Iki olivines (Ferriss et al., 2018). Estimates for bulk H^+ diffusivity in unoriented MI-bearing olivines shown by grey ellipse (Chen et al., 2011; Gaetani et al., 2012; Mironov et al., 2015; Portnyagin et al., 2008). The activation energies (E_a) and pre-exponential factors (D_0) for our best fit are provided in the inset table. (For interpretation of the references to color in this figure legend, the reader is referred to the web version of this article.)

This slope is characterised by an increase in K_2O of ~ 0.35 wt% over a drop in H_2O of 1 wt%.

The degassing-crystallization trend in K_2O-H_2O allows us to remove the effect of pre-entrapment magmatic degassing and isolate post-entrapment diffusive re-equilibration within the olivine (Lloyd et al., 2013). The amount of diffusive water loss is calculated as the difference between the observed water content in the MI and the predicted water content at entrapment, given the observed K_2O (Fig. 8). The extent of re-equilibration is then calculated as $(\text{water loss})/(\text{predicted initial } H_2O\text{-matrix } H_2O)$, where matrix H_2O is set to 0.1 wt%, reflecting the lower bound measured by nanoSIMS (Supplement).

A test for the role of diffusive water loss is whether there is a relationship between the extent of re-equilibration and MI size. During diffusive re-equilibration, smaller MIs close to the crystal edges (along \mathbf{a}_\perp) should experience the greatest extent of water loss for a given duration (Qin et al., 1992). Indeed, Fig. 9 shows that the smallest MIs have re-equilibrated to a greater extent than the larger ones. Specifically, small MIs ($<50\ \mu m$) from the 1995 eruption have lost up to 80–90 % of their entrapped H_2O . As a population, the 1995 MIs are offset to greater water loss than those from 1992. A simple explanation for this is that the 1995 olivines had more time to diffusively re-equilibrate.

6. Discussion

6.1. Modelling water loss from melt inclusions

There is a long history of modelling diffusive re-equilibration of melt inclusions with an external environment (Chen et al., 2013; Cottrell et al., 2002; Gaetani et al., 2012; Myers et al., 2019; Qin et al., 1992). These models have assumed a spherical melt inclusion in the centre of a spherical olivine and isotropic diffusion. Chen et al. (2013) coupled olivine diffusion with a degassing boundary condition in the host melt, which allows the application of their model to natural olivines in order to determine magma ascent rate.

While previous studies have used a spherical isotropic model to estimate the diffusion of H^+ through olivine, this approach is inappropriate because H^+ diffusion is strongly anisotropic with diffusion occurring approximately 1.5 orders of magnitude faster along the \mathbf{a}_\perp direction (specifically demonstrated here for Cerro Negro olivines, Fig. 5, and for others; Ferriss et al., 2018; Le Voyer et al., 2014). Numerical modelling has shown that under these circumstances, a 1D model is a better approximation of 3D anisotropic diffusion than a spherical model (Thoraval and Demouchy, 2014). It's worth noting that for Fe-Mg interdiffusion a 1D model may be problematic because

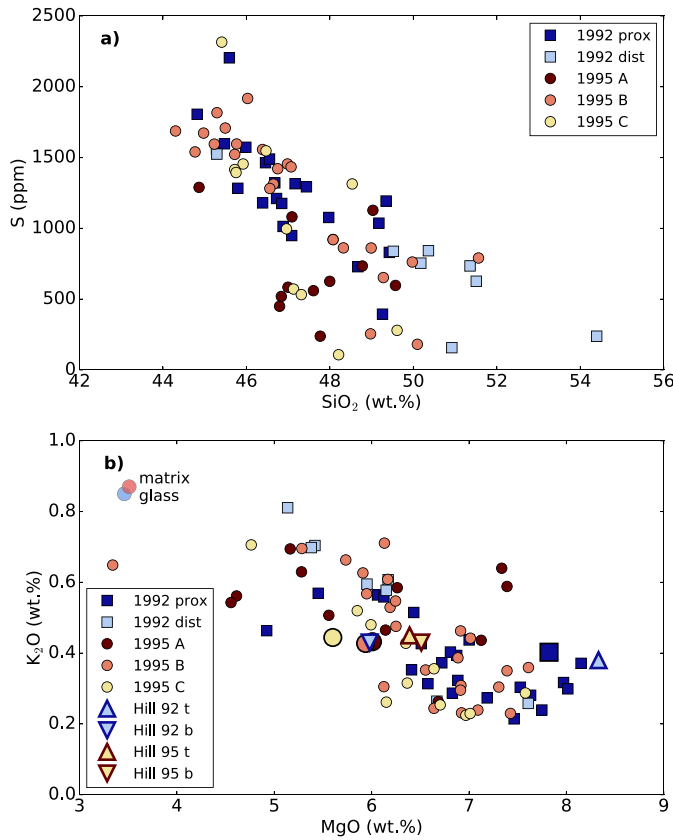


Fig. 7. Melt inclusion chemical systematics showing a) SiO₂ versus S and b) MgO versus K₂O for all samples. 1995 samples all overlap while the distal 1992 sample from peak paroxysm is shallower (lower S) and more evolved (higher SiO₂) than the proximal sample from final stage of paroxysm. Volatile-free values for SiO₂, MgO, and K₂O. Whole rock data for our 1995 samples (layers A, B, C) as well as last phase of 1992 shown in large symbols. Whole rock data from Hill et al. (1998) shown for top and bottom of 1992 and 1995 fall deposits. Matrix glass from Roggensack et al. (1997) (blue = 1995; red = 1992). (For interpretation of the references to color in this figure legend, the reader is referred to the web version of this article.)

diffusivity is less strongly anisotropic with $D_a \sim D_b \sim \frac{1}{6} D_c$ (Shea et al., 2015).

The difficulty with assuming spherical symmetry can be illustrated by considering the difference between a melt inclusion close to the edge along **c**_ and far from the edge along **a**_ versus the opposite (Fig. 10). Under the assumption of spherical symmetry, the two melt inclusions would lose water at the same rate since they have the same minimum distance from the edge. However, in reality, the melt inclusion close to the edge along **a**_ will lose water faster than the one close to the edge along **c**_ by a factor of D_a/D_c (~1.5 orders of magnitude).

We model the system as 1D diffusion along **a**_ from a melt inclusion through the olivine to a degassing boundary (Fig. 11). The inner and outer olivine boundaries are assumed to be in equilibrium with the MI and host melt, respectively, using a partition coefficient (k_D) of 0.001 (SIMS measurements in this study – Supplementary Data; Hauri et al., 2006; Le Voyer et al., 2014). The left-hand boundary is in the centre of the melt inclusion and is a no flux boundary condition. The right-hand boundary is at the olivine edge and is a Dirichlet condition with the H₂O concentration of the melt at the olivine-melt boundary calculated using Solex (Witham et al., 2012), assuming an initial H₂O of 4.7 wt% and CO₂ of 600 ppm (initial pressure of 400 MPa) (Fig. 11 and fit to data in Fig. 8b). Note that this is the maximum pressure of the model, and that each melt inclusion will record a different initial pressure determined by its inferred initial water

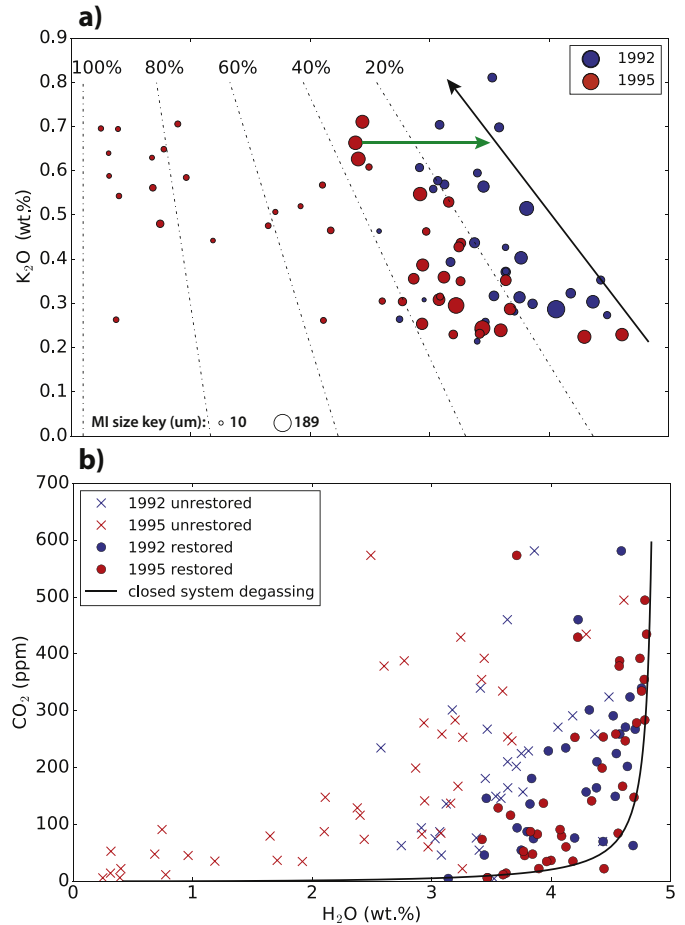


Fig. 8. (a) Degassing-induced crystallization moves melt composition upwards along the black arrow, modelled with Petrolog3 (Danyushevsky and Plechov, 2011) for starting composition of 0.26 wt% K₂O, 4.7 wt% H₂O, Pi = 3 kbar, Pf = 0.85 kbar, and decompressing at 30 bars/^oC. Measured MI H₂O is corrected back to this black line along green arrow using measured K₂O to infer pre-entrapment H₂O content. Dashed lines show amount of re-equilibration (i.e. diffusive water loss ÷ (initial water – final water)). Marker size scaled to show variation in MI size (larger markers = larger MIs). 1995 MIs have lost more water than 1992, despite extending to similar maximum water and having similar range of K₂O. (b) Crosses show measured CO₂ and H₂O concentrations, circles have been corrected for inferred diffusive water loss using method in (a). Note that 1995 and 1992 MIs extend to similar maximum CO₂ and H₂O. Black curve is calculated from Solex (Witham et al., 2012) for an initial temperature of 1100° C and initial volatile concentrations of 4.7 H₂O wt% and 600 CO₂ ppm, assuming closed system degassing with no initial vapour phase. Note that the 3 MIs to the right of the black arrow would give infinitely fast decompression rates and are excluded from the modelling – this is a limitation of the method.

content (following the solubility model in Fig. 11). Our pressure estimates are minima since we do not consider the CO₂ stored in the melt inclusion vapour bubbles. However, our model is only sensitive to magma ascent in the pressure region over which H₂O is degassing (<250 MPa), so this does not significantly affect our results. Increasing the initial CO₂ input for the Solex model from 600 to 4000 ppm only changes H₂O by <10%. Finally, the assumption of equilibrium degassing is thought to be valid for H₂O diffusion through basaltic melt, at least up to 1.5 m/s (Pichavant et al., 2013).

During development of the code, we checked that the MI-olivine-host magma system obeyed mass balance; the flux from the MI into the olivine minus the flux from the olivine into the host melt must equal the observed drop in water concentration within the olivine. We also confirmed that when spherical symmetry is used, the model results replicate those from the model in Chen et al. (2013).

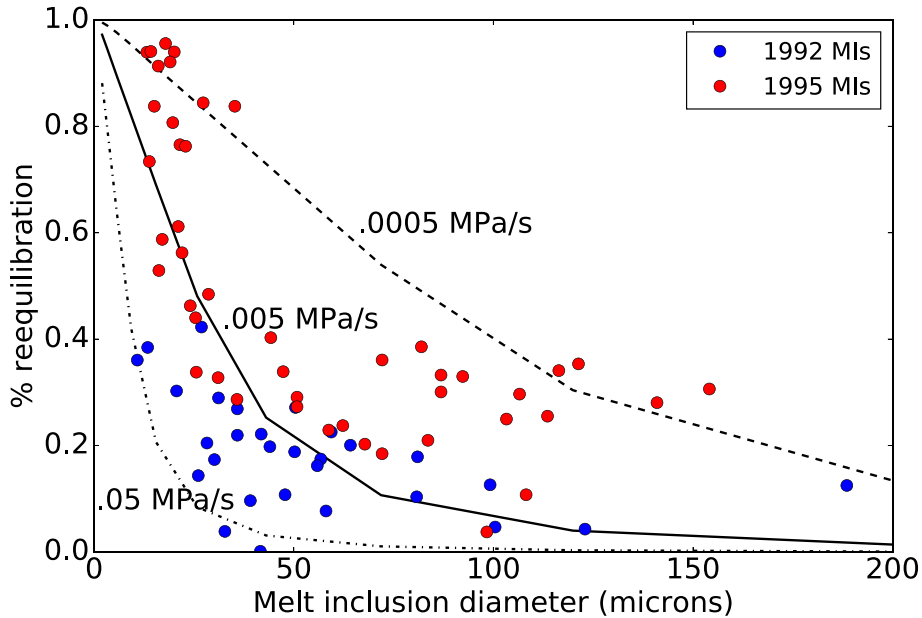


Fig. 9. Inferred H_2O re-equilibration versus melt inclusion (MI) size. Higher re-equilibration for smaller MIIs is observed, as predicted for diffusive water loss. 1995 MIIs are offset to higher re-equilibration than 1992 MIIs, suggesting longer diffusive timescales (i.e. slower ascent). Black lines show model results for different decompression rates from our 1D diffusion model assuming constant MI radius/MI-OI-edge-distance of 1/10. 1992 and 1995 MIIs are roughly separated by a decompression rate of $\sim 0.005 \text{ MPa/s}$ line. Inclusions $< 50 \mu\text{m}$ measured by NanoSIMS.

6.1.1. Uncertainty analysis

There are several sources of uncertainty in our decompression rate. As discussed in Section 5.1, there is uncertainty in the Arrhenius relationship derived from our measurements of diffusivity at 800 and 1000°C . There is also uncertainty in the temperature estimate: the average temperature from the MI population is 1100°C , which we use for the modelling, but there is a 12°C standard deviation within the range of temperature estimates. Fig. 6 shows how we combine these two uncertainties into a single uncertainty in diffusivity. Finally, the olivine-melt partition coefficient for water carries some uncertainty, as SIMS measurements of H_2O in MI and adjacent olivine give rise to a range of values for K_D (Supplementary Data).

To assess the uncertainty in our decompression rate estimates due to uncertainties in H^+ partition coefficient and diffusivity we perform Monte Carlo simulations (Press et al., 2007). For each MI,

decompression rates are estimated repeatedly based on random realizations of the two uncertain parameters, which we assume to be normally distributed with $K_D = N(0.001, 0.0003/2)$ and $\log_{10}(D_H) = N(-9.775, 0.1950/2)$, where $N(\text{mean}, \text{std})$ refers to a normal distribution. These prior distributions of K_D and D_H and further details on their rationale can be found in the Supplement.

6.2. Decompression rates

To determine decompression rate, we use our 1D numerical model of H^+ diffusion in olivine. We use the diffusivity along \mathbf{a}_\perp determined in our experiments ($10^{-9.76} \text{ m}^2/\text{s}$), corresponding to our best fit at 1100°C . Both numerical conduit models (La Spina et al., 2015) and Mg-in-melt thermometry (Newcombe et al., 2019) have found evidence for less than 20°C temperature change during ascent,

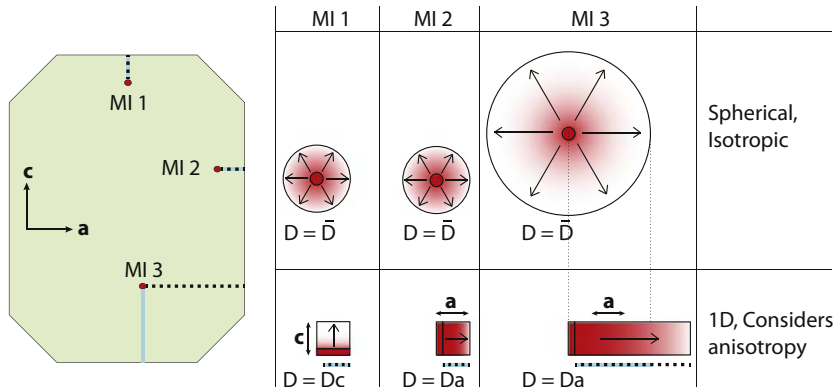


Fig. 10. Cartoon illustrating the problems with spherical symmetry and isotropic diffusivity. Left: schematic olivine with 3 MIls (red). Right: model set-up for spherical (top) and 1D (bottom) symmetry. Blue line is the distance that would be used for spherical model, dashed line is the distance used in our 1D model. MI 1 is the same distance from an olive edge as MI 2 and so would be modelled identically using a spherical model, with an isotropic diffusivity. In reality, MI 1 is close to the edge along \mathbf{c}_- whereas MI 2 is close to the edge along \mathbf{a}_- . For MI 3, the assumption of spherical symmetry leads to the use of the wrong MI-edge distance and diffusivity. (For interpretation of the references to color in this figure legend, the reader is referred to the web version of this article.)

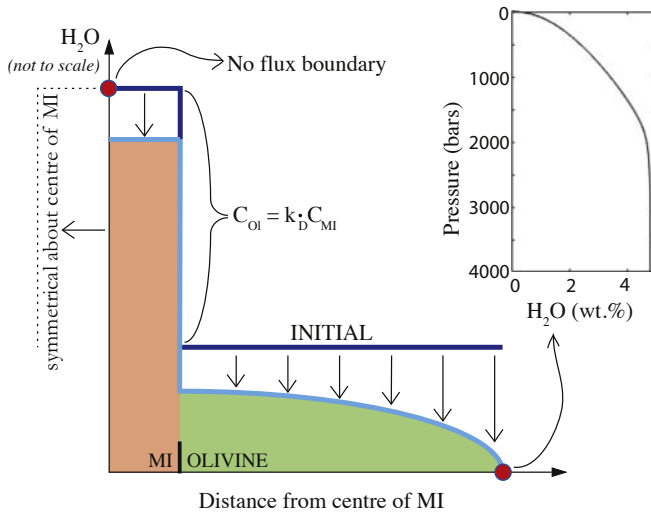


Fig. 11. Model set-up for water loss from melt inclusions. Dark blue line shows initial water concentration from centre of MI to olivine edge. Over time, olivine and MI lose water to maintain equilibrium with degassing boundary condition (from Solex Witham et al., 2012, P-H₂O trend shown inset). MI is assumed to remain in equilibrium with olivine, using a partition coefficient of 0.001 (Hauri et al., 2006; Le Voyer et al., 2014). (For interpretation of the references to color in this figure legend, the reader is referred to the web version of this article.)

which is within our uncertainty on temperature (Section 6.1.1), and so we assume isothermal ascent. Fig. 12 shows the results from the models. On average, the 1992 MIs record faster decompression than the 1995 MIs. Since there is some skew to the data, the median values are probably a better reflection of the average than the mean. They indicate a 5-fold faster ascent for the 1992 olivines (0.0073 versus 0.0014 MPa/s). A comparison between results from our 1D model and a spherically-symmetric model preserves this difference between 1992 and 1995 MIs, but shows that the isotropic spherical model consistently under-predicts the decompression rate on average by a factor of 3, and up to a factor of 8 for individual samples (Supplement).

Monte Carlo simulations show that each MI has a log-normal distribution of decompression rate with 2σ uncertainty in $\log(dP/dt)$ of $\sim 10\%$ (Fig. 12). This is much smaller than the order of magnitude spread in decompression rate within each eruption, which suggests that there is real variation in decompression rate for a given deposit. This is possibly a manifestation of the cross-conduit velocity profile of the magma, with faster moving material in the centre and slower material at conduit edges, as has been proposed on the basis of both modelling and textural studies of erupted clasts (e.g. Collier and Neuberg, 2006; Sable et al., 2006). Some of the spread in decompression rates could also come from variations in initial water that are not captured by our assumption of initial water from the degassing-crystallization trend shown in Fig. 8.

To summarize, we find that the magma decompression rate during the 1992 VEI 3 eruption was faster than during the 1995 VEI 2 eruption. This places the boundary between VEI 2 and 3 intensities at a decompression rate of about 0.005 MPa/s. Assuming a magma density of 2600 kg m^{-3} and a conduit radius of 5 m, this corresponds to an ascent rate of $\sim 0.1 \text{ m/s}$ and a mass eruption rate of $\sim 10^4 \text{ kg/s}$. As we discuss in Section 6.3, this may correspond to the transition from purely explosive to dual effusive-explosive behaviour in basaltic eruptions.

6.2.1. Non-linear decompression

A common assumption made in volatile diffusion modelling is constant decompression rate. Conduit models indicate that magma

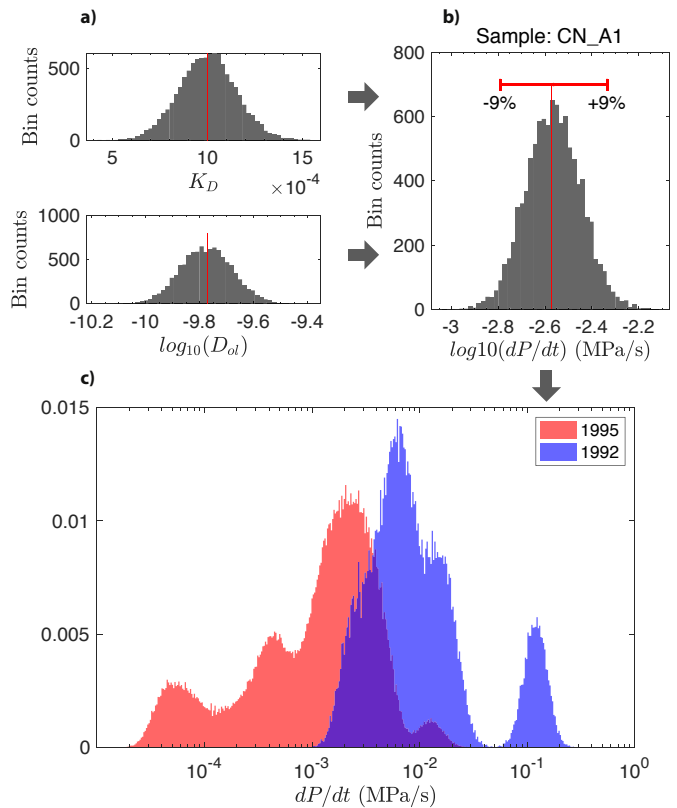


Fig. 12. Results from Monte Carlo simulations. (a) Prior distributions for D_{Ol} and K_D for an example MI (1995 CN A1). (b) Posterior distribution of decompression rate for the same example MI. Red bar indicates $\pm 2\sigma$ (c) Distribution of combined posterior decompression rates for all MIs (1992: blue, 1995: red). (For interpretation of the references to color in this figure legend, the reader is referred to the web version of this article.)

decompression will likely accelerate because of the expansion of volatiles and increase in frictional pressure loss as magma becomes drier and more viscous at shallow depths (e.g. Gonnermann and Manga, 2007). We use our 1D diffusion model to explore the effect of non-linear decompression on inferred ascent times. Following the method of Su and Huber (2017), we parameterize the decompression path using two parameters: the total ascent time (τ) and degree of non-linearity (γ):

$$\frac{dP}{dt} = -\frac{\gamma P_i e^{\frac{\gamma t}{\tau}}}{\tau(e^\gamma - 1)} \quad (3)$$

where P_i is the initial pressure and t is time. When $\gamma \rightarrow 0$, the decompression rate becomes linear with $\frac{dP}{dt} = -\frac{P_i}{\tau}$. With $\gamma > 0$, the magma accelerates as it rises and the magnitude of this acceleration increases with γ (see inset Fig. 13).

Eq. (3) implies a strong trade-off between degree of non-linearity (γ) and total ascent time (τ), which is also shown in Fig. 13. The greater the degree of acceleration (higher γ), the longer the duration of ascent (higher τ) in order to match initial and final MI water concentration (black strip at zero misfit). This can be understood by considering that water solubility is pressure dependent and water loss occurs mostly at shallower depths (Fig. 11). The higher γ , the less time spent at shallow depths, which is compensated by a longer total time.

In agreement with Su and Huber (2017), we find that models which consider linear decompression will significantly underestimate total magma ascent time. For example, a melt inclusion from 1992 with an ascent time of $\sim 3 \text{ h}$ under linear decompression would

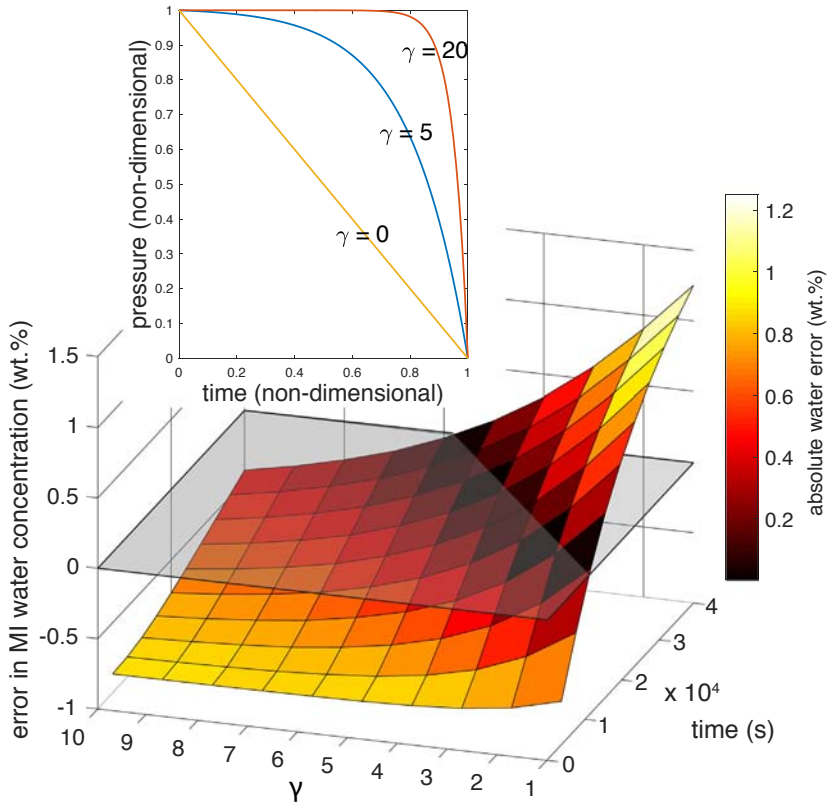


Fig. 13. Misfit plot showing error in estimated MI water content for a range of γ (non-linearity) and total ascent times. For clarity, grey surface shows the plane of zero error; black strip at $z = 0$ corresponds to best fit combinations of γ and t . Note that colouring is for absolute error, whereas the z axis shows the actual error (i.e. whether the model over- or under-predicts MI water content.) Inset shows parameterization of decompression path. As $\gamma \rightarrow 0$ the decompression becomes linear. $\gamma = 20$ gives highly nonlinear decompression. (For interpretation of the references to color in this figure legend, the reader is referred to the web version of this article.)

require ~ 10 h if $\gamma = 5$. While we are not currently in a position to constrain γ for real eruptions, this exercise highlights a future avenue for research: to couple diffusion models with conduit models.

6.3. What drove the different eruptive styles of the 1992 and 1995 eruptions?

Now we turn to the question of what caused the difference in explosive styles of the 1992 VEI 3 and 1995 VEI 2 eruptions. Many factors play into the dynamics of eruptions, including but not limited to: viscosity, bubble and crystal nucleation and growth, deformation of the magma, decompression rate and conduit radius and shape (Cassidy et al., 2018; Gonnermann and Manga, 2013). These factors tend to affect each other and thus complex feedbacks arise.

Due to their fundamental role in driving explosive eruptions, volatiles are often called upon to explain differences in eruptive styles (Andújar and Scaillet, 2012). Magmas with higher volatile contents have higher potential energy to convert into kinetic energy through the exsolution and expansion of bubbles, and so should erupt more explosively than those with lower volatiles. As the most volumetrically important volatile, it follows that initial dissolved H_2O could control explosivity. However, no correlation has been found in comparisons of VEI and maximum H_2O concentrations in MIs (Cassidy et al., 2018; Ferguson et al., 2016; Koleszar et al., 2012). Indeed, in our data for Cerro Negro, MIs from the 1992 and 1995 eruptions contain similar maximum volatile concentrations of ~ 4.7 wt% H_2O (Fig. 8). We therefore think it is unlikely that variations in initial volatile concentration play any major role in setting the explosive style.

However, the style of degassing should play a major role in setting the style of eruption (Edmonds, 2008; Jaupart and Allègre, 1991; Parfitt and Wilson, 1994). When bubbles and melt are coupled, bubbles act to accelerate the magma towards explosive fragmentation. If, on the other hand, bubbles can separate from the magma, the magma's buoyancy is reduced, as is the driving force for an explosive eruption. The behaviour of bubbles within the magma depends on bubble size and number density, magma rheology (which is itself affected by bubble size and number density), the depth of exsolution, and the magma ascent rate (Gonnermann and Manga, 2013). Thus, decompression rate both controls and depends on the degassing style.

As well as having lower plume height and mass eruption rate, the 1995 eruption effused lava during its pyroclastic activity, while the 1992 eruption was purely explosive (Section 3, Hill et al., 1998). This behaviour of the 1995 eruption is not unusual; there is a tendency for violent Strombolian eruptions to be accompanied by lava flows. Concurrent effusive and explosive activity points towards separated flow of bubbles and melt. Modelling (Pioli et al., 2009) and experiments (Menand and Phillips, 2007) have shown that this duality of behaviour is largely controlled by the mass eruption rate (MER), and is only possible for an intermediate range of MER. Too slow and the magma loses all its volatiles; too fast and the bubbles remain completely trapped within the magma.

Our work supports this notion that mass eruption rate exerts a fundamental control on the eruptive style. We show that the 1995 MIs record higher extents of diffusive water loss than 1992 MIs (Fig. 9) and our diffusion modelling attributes this to differences in magma decompression rate. We argue that the most straightforward

explanation for the difference in explosive style is that the 1995 magma rose slower than that of the 1992 eruption, allowing for some amount of segregation of bubbles and melt, thereby reducing the explosivity of the pyroclastic activity. This reasoning would place the critical decompression rate separating purely explosive eruptions from effusive-explosive eruptions at ~ 0.005 MPa/s, corresponding to a mass eruption rate of $\sim 10^4$ kg/s, which agrees well with the modelling by Pioli et al. (2009) (their Fig. 7).

6.3.1. Continuous ascent or shallow stalling?

The cause for the difference in explosivity of the 1992 and 1995 Cerro Negro eruptions was previously attributed to shallow stalling of the 1995 magma, allowing for the escape of volatiles (Roggensack et al., 1997; Venugopal et al., 2016). We observe more water loss on average in MIs from the 1995 eruption. Shallow escape of a vapour phase in the 1995 magma may have reduced the driving force for an explosive eruption. Was this vapour phase lost during shallow stalling or simply slow ascent? The key observation here is that the 1995 and 1992 MIs extend to the same maximum H₂O. This precludes a shallow stalling event because H⁺ diffusion in olivine is fast and would reset MIs to a lower water concentration, erasing any evidence of an initially high H₂O magma. Furthermore, a stalling event would reset all of the inclusions to a new water content but would not affect the K₂O, forming a vertical array on the H₂O-K₂O plot. Yet the larger, high water MIs from 1995 do not reflect a common water content – some have 3.5 and some have 2.5 wt% H₂O. Instead, they appear to form an inclined array, paralleling the 1992 inclusions and the magma fractionation trend (Fig. 8). This is inconsistent with a shallow stalling event, but entirely consistent with slower ascent. Therefore, the most straightforward explanation is that the two magmas had the same parental composition and that the 1995 magma ascended slowly enough to diffusively lose water from its smaller MIs. When saturation pressures are calculated using the corrected H₂O concentrations, the two magmas are identical, and the

differences reported by Roggensack et al. (1997) collapse to a single trend (see Supplement).

6.4. Other eruptions

Our results support the hypothesis that decompression rate plays a major role in setting the explosivity of eruptions at basaltic to intermediate volcanoes. Magma from the VEI 3 eruption of 1992 decompressed at a rate of ~ 0.0073 MPa/s (~ 0.3 m/s), while magma from the VEI 2 1995 eruption record decompression rates of ~ 0.0014 MPa/s (~ 0.05 m/s). These decompression rates fit within the general trend of mass eruption rate (MER) versus decompression rate based on embayment studies for other volcanoes (Fig. 14). The embayment method uses concentration profiles of volatile species with different diffusivities (C, S, H) along melt embayments to model decompression rate (Humphreys et al., 2008; Lloyd et al., 2014). Its advantage over the melt inclusion method is that it relies on diffusivities in melt which are better constrained than in olivine and are isotropic. However, embayments can be exceedingly rare in some samples (including the 1992 and 1995 Cerro Negro eruptions). Further difficulty with embayments is the possibility of multicomponent diffusion effects (Newcombe et al., 2014; Zhang et al., 2010), as well as the effects of often complex 3D morphologies of embayments which have not yet been characterised.

The 1977 Seguam and 1959 Kilauea Iki eruptions share a similar MER with the 1992 Cerro Negro eruption and embayment studies have yielded decompression rates for these two eruptions that are similar to our decompression rates for the 1992 eruption. These three eruptions all have about one order of magnitude slower decompression rate than the higher intensity eruptions of Fuego 1974 and Kilauea Keanakakoi (0.4–0.45 MPa/s). The 1995 Cerro Negro eruption has the lowest MER of any volcano for which there exists a decompression rate estimate, and the decompression rate we estimate is the lowest of all eruptions analysed (<0.005 MPa/s).

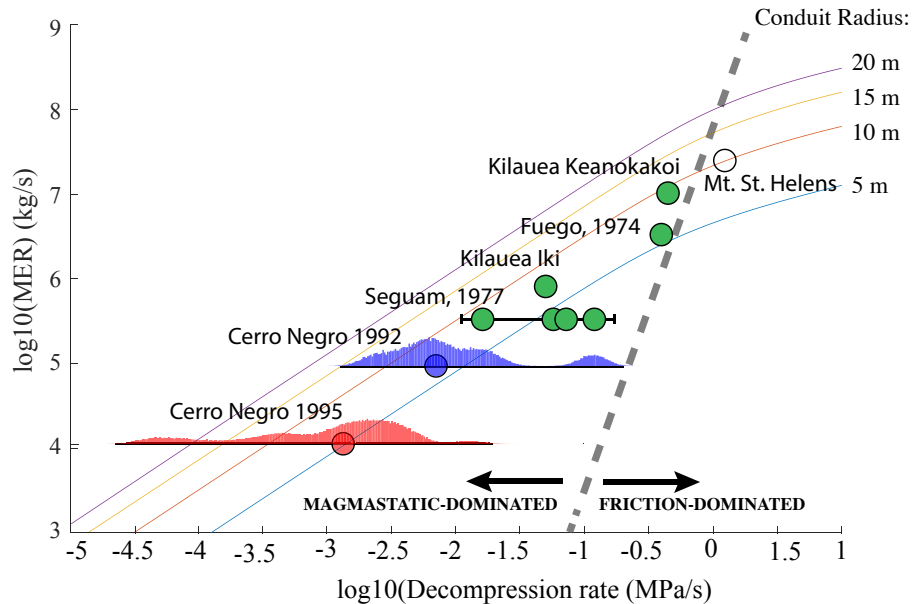


Fig. 14. Mass eruption rate versus decompression rate for range of eruptions. Lines are solutions to simple conduit flow model with constant conduit radius. Cerro Negro dP/dt from this study, all others from embayment studies (Ferguson et al., 2016; Humphreys et al., 2008; Newcombe et al., 2017). Mt. St. Helens shown in open symbol since it is a silicic eruption and may be governed by different processes. Monte Carlo distributions for Cerro Negro (shown in Fig. 12) overlain in red (1995) and blue (1992) shading, red and blue circles show median values. MER estimates from total volume and eruption time or plume height via direct observation or dispersal mapping (Seguam – volume mapping – Terry Plank, pers. comm.; Mt. St. Helens – plume height – Humphreys et al. (2008); Fuego – volume mapping – Rose et al. (2008); Kilauea Iki – plume height – Richter et al. (1970); Kilaeua Keanakakoi – volume mapping; Cerro Negro – volume mapping – Hill et al. (1998), Pioli et al. (2009)). (For interpretation of the references to color in this figure legend, the reader is referred to the web version of this article.)

For a simple pipe-flow model, there is a theoretical relationship between MER, decompression rate and conduit radius that is given by:

$$\frac{dP}{dt} = \frac{-u}{1 - M^2} \cdot \left(\rho g + \frac{\rho(u^2)f}{a} \right) \quad (4)$$

where u is magma ascent rate (m/s), M is the Mach number relating u to the speed of sound in the magma ($M = \frac{u^2}{c^2}$), ρ is the magma density (kg m^{-3}), f is the friction factor, and a is the conduit diameter (m) (e.g. Gonnermann and Manga, 2013). Mass eruption rate (Q) relates to this equation through the magma ascent rate, by conservation of mass:

$$Q = \rho u A \quad (5)$$

where A is the cross-sectional conduit area (m^2).

We calculate MER as a function of decompression rate for different assumed conduit sizes and overlay these curves on the data (Fig. 14). The curves show a change in slope at $\sim 0.1\text{--}1 \text{ MPa/s}$ between magmatic- and friction-dominated decompression at low and high decompression rates respectively (grey dashed line). The two Cerro Negro eruptions are well within the magmatic dominated regime, as might be expected for its relatively low viscosity basaltic magma ($\sim 10^2 \text{ Pa s}$).

Under the assumption of a cylindrical conduit geometry, all eruptions appear well described by a conduit radius of 5–10 m (Fig. 14). However, the concept of a conduit radius is probably only meaningful at shallow depths, while at deeper levels, a dyke geometry is more likely. For the same cross sectional area, magma flow in a dyke would have a higher decompression rate for a given mass eruption rate, since there is more surface area for frictional pressure loss.

The trend in the data is following the predicted theoretical relationship between mass eruption rate and decompression rate. But what causes the spread in the data? What is the underlying phenomenon that drives the 1992 eruption to have higher MER and decompression rate than the 1995 eruption? In some cases, rapid surface unloading (e.g. landslide at Mount St. Helens; Alibirov and Dingwell, 1996) is responsible for fast decompression rate by causing a near-instantaneous decompression in the magma column. However, this is not a general mechanism as many explosive eruptions show no evidence for a catastrophic unloading event (Goepfert and Gardner, 2010), including the 1992 and 1995 eruptions at Cerro Negro (La Femina et al., 2004; McClelland, 1992; Wunderman, 1995). Another possibility is that high dissolved CO_2 concentrations in the magma could cause deep exsolution and early buoyancy (Lowenstein, 2001). While we see no evidence for a difference in the maximum volatile concentrations of the 1992 and 1995 magmas, deep exsolution of a CO_2 -rich gas phase before crystallization could mean that high CO_2 concentrations were never captured in the melt inclusions. Finally, it is possible that small variations in the chamber overpressure at the initiation of the eruption could control decompression rate. Assuming a viscoelastic wall rock rheology, a higher chamber overpressure would create a wider dyke which in turn would increase the mass eruption rate and decompression rate (Bokhove et al., 2005). Different chamber overpressures would presumably be related to different wall rock strengths, as well as the size of the chamber and the input rate of magma or gas from depth (Degruyter and Huber, 2014). Our work is not able to distinguish between these scenarios. Future studies into the root cause(s) behind differences in MER and decompression rate would benefit greatly from combining conduit modelling and petrology with gas and geodetic monitoring, which can help to infer the depth and magnitude of the source of overpressure.

7. Conclusions

We have measured the fastest H^+ diffusivity on record for dehydrating olivine. This may be linked to the fact that the Cerro Negro olivines studied here are the lowest forsterite olivines that have been experimentally dehydrated, since Fe is expected to facilitate quick exchange of electrons between defects. We believe that these diffusivities are relevant for olivine phenocrysts with $\text{Fo} 70\text{--}80$, common to many basaltic/andesitic eruptions. It is possible that olivines with lower Fo will show even faster H^+ diffusion. High diffusivities imply that only the largest inclusions ($>100 \mu\text{m}$) located far from the crystal edge can entirely avoid diffusive water loss during VEI 2–3 eruptions. It is therefore important to measure MI size and distance from the olivine edge (along \mathbf{a}_\perp) when working with MIs in order to assess MI fidelity. Significant water loss ($>20\%$) occurs in melt inclusions smaller than $\sim 100 \mu\text{m}$ for the 1995 VEI 2 eruption and $\sim 40 \mu\text{m}$ for the 1992 VEI 3 eruption of Cerro Negro. Higher intensity eruptions are likely to preserve initial MI H_2O concentrations for even smaller melt inclusions.

Due to the strong anisotropy of H^+ diffusion in olivine, water loss from melt inclusions is dominated by diffusion along \mathbf{a}_\perp . Thus, a 1D diffusion model oriented along \mathbf{a}_\perp is more accurate than a spherical, isotropic diffusion model. 1D diffusion modelling oriented along the fast \mathbf{a}_\perp direction, combined with our newly determined diffusivity, indicates that magma from the VEI 3 eruption of 1992 ascended at a rate of roughly 0.0073 MPa/s , $\sim 5\times$ faster than that from the 1995 VEI 2 eruption. Assuming linear decompression, the 1992 magma ascended from 5–10 km in $\sim 6.5 \text{ h}$ while it took the 1995 magma $\sim 35 \text{ h}$. These are conservatively low estimates for the total ascent time because magma is expected to accelerate to the surface. Monte Carlo simulations give a 2σ uncertainty on $\log_{10}(dp/dt)$ for each MI of $\sim 10\%$ – much smaller than the order of magnitude spread in decompression rate within each eruption, which suggests that there is real variation in decompression rate for a given deposit. The higher decompression rate for the 1992 eruption is correlated with a more explosive eruption, perhaps due to increased coupling of bubbles and magma.

Our results build on a growing number of decompression rate estimates from embayment studies. They demonstrate the strength of using diffusive water loss from olivine-hosted melt inclusions when embayments are not a viable option. While we find no link between initial water concentration and eruption style, a clear correlation is emerging between mass eruption rate, eruptive style and decompression rate. This supports a shift in view away from the idea that initial H_2O concentration controls eruption style.

Acknowledgments

We would like to acknowledge Kurt Roggensack for his insightful input at the beginning of the project and Michael Carr, who provided the 1992 samples. We appreciate the technical support of Adrian Fiege at the AMNH during the electron probe data collection, Louis Bolge during the LA-ICP-MS data collection, and Jianhua Wang at CIW during SIMS and nanoSIMS data collection. We are grateful to help from Dave Walker in performing the diffusion experiments and Elizabeth Ferriss for her whole-block codes. We thank Philipp Ruprecht, Thomas Shea and an anonymous reviewer for helpful comments that led to clarity and depth to our presentation and arguments. This work was supported by NSF Award No. EAR-1524542.

Appendix A. Supplementary data

Supplementary data to this article can be found online at <https://doi.org/10.1016/j.jvolgeores.2019.106664>.

References

- Alidibirov, M., Dingwell, D., 1996. An experimental facility for the investigation of magma fragmentation by rapid decompression. *Bull. Volcanol.* 58, 411–416.
- Andújar, J., Scaillet, B., 2012. Relationships between pre-eruptive conditions and eruptive styles of phonolite-trachyte magmas. *Lithos* 152, 122–131.
- Bell, D.R., Rossman, G.R., Maldener, J., Endisch, D., Rauch, F., 2003. Hydroxide in olivine: a quantitative determination of the absolute amount and calibration of the IR spectrum. *J. Geophys. Res. Solid Earth* 108 (B2).
- Beran, A., 1969. Über OH-gruppen in Olivin. Österreich Akademie Des Wissenschaften.
- Berry, A.J., Hermann, J., O'Neill, H.S.C., Foran, G.J., 2005. Fingerprinting the water site in mantle olivine. *Geology* 33 (11), 869–872.
- Bokhove, O., Woods, A.W., De Boer, A., 2005. Magma flow through elastic-walled dikes. *Theor. Comput. Fluid Dyn.* 19 (4), 261–286.
- Cashman, K.V., 2004. Volatile controls on magma ascent and eruption. *State Planet Front. Chall. Geophys. Geophys.* 19, 109–124.
- Cassidy, M., Manga, M., Cashman, K., Bachmann, O., 2018. Controls on explosive-effusive volcanic eruption styles. *Nat. Commun.* 9 (1).
- Chen, Y., Provost, A., Schiano, P., Cluzel, N., 2011. The rate of water loss from olivine-hosted melt inclusions. *Contrib. Mineral. Petro.* 162 (3), 625–636.
- Chen, Y., Provost, A., Schiano, P., Cluzel, N., 2013. Magma ascent rate and initial water concentration inferred from diffusive water loss from olivine-hosted melt inclusions. *Contrib. Mineral. Petro.* 165 (3), 525–541.
- Collier, L., Neuberger, J., 2006. Incorporating seismic observations into 2D conduit flow modeling. *J. Volcanol. Geotherm. Res.* 152 (3–4), 331–346.
- Costa, A., Melnik, O., Vedeneva, E., 2007. Thermal effects during magma ascent in conduits. *J. Geophys. Res. Solid Earth* 112 (12), 1–16.
- Costa, F., Chakraborty, S., 2008. The effect of water on Si and O diffusion rates in olivine and implications for transport properties and processes in the upper mantle. *Phys. Earth Planet. Inter.* 166 (1–2), 11–29.
- Cottrell, E., Spiegelman, M., Langmuir, C.H., 2002. Consequences of diffusive reequilibration for the interpretation of melt inclusions. *Geochem. Geophys. Geosyst.* 3 (5), 1–26.
- Crank, J., 1975. *The Mathematics of Diffusion*: 2d Ed. Clarendon Press.
- Danyushevsky, L.V., Della, F.N., Sokolov, S., 2000. Re-equilibration of Melt Inclusions Trapped by Magnesian Olivine Phenocrysts from Subduction-related Magmas: Petrological Implications. , pp. 68–83.
- Danyushevsky, L.V., Plechov, P., 2011. Petrolog3: integrated software for modeling crystallization processes. *Geochem. Geophys. Geosyst.* 12 (7).
- DeGruyter, W., Huber, C., 2014. A model for eruption frequency of upper crustal silicic magma chambers. *Earth Planet. Sci. Lett.* 403, 117–130.
- Demouchy, S., Mackwell, S., 2006. Mechanisms of hydrogen incorporation and diffusion in iron-bearing olivine. *Phys. Chem. Miner.* 33 (5), 347–355.
- Edmonds, M., 2008. New geochemical insights into volcanic degassing. *Philos. Trans. R. Soc. A Math. Phys. Eng. Sci.* 366 (1885) 4559 LP – 4579.
- Eichelberger, J.C., Westrich, H.R., 2012. Magmatic volatiles in explosive rhyolitic eruptions. *Geophys. Res. Lett.* 8 (7), 757–760.
- Ferguson, D.J., Gonnermann, H.M., Ruprecht, P., Plank, T., Hauri, E.H., Houghton, B.F., Swanson, D.A., 2016. Magma decompression rates during explosive eruptions of Kīlauea volcano, Hawaii, recorded by melt embayments. *Bull. Volcanol.* 78 (10).
- Ferriss, E., Plank, T., Newcombe, M., 2018. Site-specific dehydration of olivines from San Carlos and Kīlauea Iki. Submitted. (1).
- Ferriss, E., Plank, T., Walker, D., 2016. Site-specific hydrogen diffusion rates during clinopyroxene dehydration. *Contrib. Mineral. Petro.* 171 (6), 1–24.
- Ferriss, E., Plank, T., Walker, D., Nettles, M., 2015. The whole-block approach to measuring hydrogen diffusivity in nominally anhydrous minerals. *Am. Mineral.* 100 (4), 837–851.
- Gaetani, G.A., O'Leary, J.A., Shimizu, N., Bucholz, C.E., Newville, M., 2012. Rapid reequilibration of H₂O and oxygen fugacity in olivine-hosted melt inclusions. *Geology* 40 (10), 915–918.
- Geschwind, C.H., Rutherford, M.J., 1995. Crystallization of microlites during magma ascent: the fluid mechanics of 1980–1986 eruptions at Mount St Helens. *Bull. Volcanol.* 57 (5), 356–370.
- Goepfert, K., Gardner, J.E., 2010. Influence of pre-eruptive storage conditions and volatile contents on explosive Plinian style eruptions of basic magma. *Bull. Volcanol.* 72 (5), 511–521.
- Gonnermann, H.M., Manga, M., 2007. The fluid mechanics inside a volcano. *Annu. Rev. Fluid Mech.* 39 (1), 321–356.
- Gonnermann, H.M., Manga, M., 2013. Dynamics of magma ascent in the volcanic conduit. *Modeling Volcanic Processes: The Physics and Mathematics of Volcanism*, , pp. 55–84.
- Hauri, E., Wang, J., Dixon, J.E., King, P.L., Mandeville, C., Newman, S., 2002. SIMS analysis of volatiles in silicate glasses: 1. Calibration, matrix effects and comparisons with FTIR. *Chem. Geol.* 183 (1–4), 99–114.
- Hauri, E.H., Gaetani, G.A., Green, T.H., 2006. Partitioning of water during melting of the Earth's upper mantle at H₂O-undersaturated conditions. *Earth Planet. Sci. Lett.* 248 (3–4), 715–734.
- Hill, B.E., Connor, C.B., Jarzemba, M.S., La Femina, P.C., Navarro, M., Strauch, W., 1998. 1995 eruptions of Cerro Negro volcano, Nicaragua, and risk assessment for future eruptions. *Bull. Geol. Soc. Am.* 110 (10), 1231–1241.
- Humphreys, M.C.S., Menand, T., Blundy, J.D., Klimm, K., 2008. Magma ascent rates in explosive eruptions: constraints from H₂O diffusion in melt inclusions. *Earth Planet. Sci. Lett.* 270 (1–2), 25–40.
- Ingrin, J., Hercule, S., Charton, T., 1995. Diffusion of hydrogen in diopside: results of dehydration experiments. *J. Geophys. Res.* 100 (B8), 15489–15499.
- Jaupart, C., Allègre, C.J., 1991. Gas content, eruption rate and instabilities of eruption regime in silicic volcanoes. . *Letters, Planetary Science V* 102. Elsevier Science Publishers B., pp. 413–429.
- Kohlstedt, D.L., Mackwell, S.J., 1998. Diffusion of hydrogen and intrinsic point defects in olivine. *Z. Phys. Chem.* 207, 147–162.
- Koleszar, A.M., Kent, A.J., Wallace, P.J., Scott, W.E., 2012. Controls on long-term low explosivity at andesitic arc volcanoes: insights from Mount Hood, Oregon. *J. Volcanol. Geotherm. Res.* 219–220, 1–14.
- Kress, V.C., Carmichael, I.S.E., 1991. The compressibility of silicate liquids containing Fe₂O₃ and the effect of composition, temperature, oxygen fugacity and pressure on their redox states. *Contrib. Mineral. Petro.* 108 (1–2), 82–92.
- La Femina, P.C., Connor, C.B., Hill, B.E., Strauch, W., Saballos, J.A., 2004. Magma-tectonic interactions in Nicaragua: the 1999 seismic swarm and eruption of Cerro Negro volcano. *J. Volcanol. Geotherm. Res.* 137 (1–3 SPEC. ISS.), 187–199.
- La Spina, G., Burton, M., de' Micheli Vitturi, M., 2015. Temperature evolution during magma ascent in basaltic effusive eruptions: a numerical application to Stromboli volcano. *Earth Planet. Sci. Lett.* 426, 89–100.
- Le Voyer, M., Asimow, P.D., Mosenfelder, J.L., Guan, Y., Wallace, P., Schiano, P., Stolper, E.M., Eiler, J.M., 2014. Zonation of H₂O and F concentrations around melt inclusions in olivines. *J. Petrol.* 55 (4), 685–707.
- Lloyd, A.S., Plank, T., Ruprecht, P., Hauri, E.H., Rose, W., 2013. Volatile loss from melt inclusions in pyroclasts of differing sizes. *Contrib. Miner. Petro.* 165 (1), 129–153.
- Lloyd, A.S., Ruprecht, P., Hauri, E.H., Rose, W., Gonnermann, H.M., Plank, T., 2014. NanoSIMS results from olivine-hosted melt embayments: magma ascent rate during explosive basaltic eruptions. *J. Volcanol. Geotherm. Res.* 283, 1–18.
- Lowenstein, J.B., 2001. Carbon dioxide in magmas and implications for hydrothermal systems. *Mineral. Deposita* 36 (6), 490–502.
- McClelland, L. e., 1992a. Global Volcanism Program, 1992. Report on Cerro Negro (Nicaragua). Technical report. Bulletin of the Global Volcanism Network, 17:4. Smithsonian Institution.
- Menand, T., Phillips, J.C., 2007. Gas segregation in dykes and sills. *J. Volcanol. Geotherm. Res.* 159 (4), 393–408.
- Mironov, N., Portnyagin, M., Botcharnikov, R., Gurenko, A., Hoernle, K., Holtz, F., 2015. Quantification of the CO₂ budget and H₂O-CO₂ systematics in subduction-zone magmas through the experimental hydration of melt inclusions in olivine at high H₂O pressure. *Earth Planet. Sci. Lett.* 425, 1–11.
- Myers, M.L., Wallace, P.J., Wilson, C.J., 2019. Inferring magma ascent timescales and reconstructing conduit processes in explosive rhyolitic eruptions using diffusive losses of hydrogen from melt inclusions. *J. Volcanol. Geotherm. Res.* 369, 95–112.
- Newcombe, M.E., Asimow, P.D., Ferriss, E., Barth, A., Lloyd, A.S., Hauri, E., Plank, T.A., 2017. Water-in-Olivine Magma Ascent Chronometry: Every Crystal is a Clock. AGU Fall Meeting Abstracts.
- Newcombe, M.E., Fabrizio, A., Zhang, Y., Ma, C., Le Voyer, M., Guan, Y., Eiler, J.M., Saal, A.E., Stolper, E.M., 2014. Chemical zonation in olivine-hosted melt inclusions. *Contrib. Mineral. Petro.* 168 (1), 1030.
- Newcombe, M.E., Plank, T., Zhang, Y., Lloyd, A., Ferguson, D., Barth, A., 2019. Syneruptive pressure-temperature-time paths of basaltic magma. AGU Fall Meeting Abstracts.
- Ni, P., Zhang, Y., Guan, Y., 2017. Volatile loss during homogenization of lunar melt inclusions. *Earth Planet. Sci. Lett.* 478, 214–224.
- Padrón-Navarta, J.A., Hermann, J., O'Neill, H.S.C., 2014. Site-specific hydrogen diffusion rates in forsterite. *Earth Planet. Sci. Lett.* 392, 100–112.
- Parfitt, E.A., Wilson, L., 1994. Modelling the transition between Hawaiian-style lava fountaining and Strombolian explosive volcanic activity. Abstracts of the 25th Lunar and Planetary Science Conference. pp. 1049–1050. (1 995).
- Peslier, A.H., Bizimis, M., Matney, M., 2015. Water disequilibrium in olivines from Hawaiian peridotites: recent metasomatism, H diffusion and magma ascent rates. *Geochim. Cosmochim. Acta* 154, 98–117.
- Pichavant, M., Di Carlo, I., Rotolo, S.G., Scaillet, B., Burgisser, A., Le Gall, N., Martel, C., 2013. Generation of CO₂-rich melts during basalt magma ascent and degassing. *Contrib. Mineral. Petro.* 166 (2), 545–561.
- Portnyagin, M.V., Hoernle, K., Mironov, N.L., 2014. Contrasting compositional trends of rocks and olivine-hosted melt inclusions from Cerro Negro volcano (Central America): implications for decompression-driven fractionation of hydrous magmas. *Int. J. Earth Sci.* 103 (7), 1963–1982.
- Press, W.H., Teukolsky, S.A., Vetterling, W.T., Flannery, B.P., 2007. *Numerical Recipes 3rd Edition: The Art of Scientific Computing*. Cambridge University Press.
- Putirka, K.D., Perfit, M., Ryerson, F.J., Jackson, M.G., 2007. Ambient and excess mantle temperatures, olivine thermometry, and active vs. passive upwelling. *Chem. Geol.* 241 (3–4), 177–206.
- Qin, Z., Lu, F., Anderson, A.T., 1992. Diffusive reequilibration of melt and fluid inclusions. *Am. Mineral.* 77 (5–6), 565–576.
- Richter, D., Eaton, J., Murata, K., Ault, W., Krivoy, H., 1970. Chronological narrative of the 1959–60 eruption of Kīlauea Volcano, Hawaii. U.S. Geological Survey Professional Paper 537-E. pp. E1–E73.
- Roggensack, K., Hervig, R.L., McKnight, S.B., Stanley, N., Williams, S.N., 1997. Explosive basaltic volcanism from Cerro Negro Volcano: influence of volatiles on eruptive style. *Science* 277 (5332), 1639–1642.

- Rose, W.I., Self, S., Murrow, P.J., Bonadonna, C., Durant, A.J., Ernst, G.G.J., 2008. Nature and significance of small volume fall deposits at composite volcanoes: insights from the October 14, 1974 Fuego eruption, Guatemala. *Bull. Volcanol.* 70 (9), 1043–1067.
- Sable, J.E., Houghton, B.F., Del Carlo, P., Coltelli, M., 2006. Changing conditions of magma ascent and fragmentation during the Etna 122 BC basaltic Plinian eruption: evidence from clast microtextures. *J. Volcanol. Geotherm. Res.* 158 (3–4), 333–354.
- Shea, T., Costa, F., Krimer, D., Hammer, J.E., 2015. Accuracy of timescales retrieved from diffusion modeling in olivine: a 3D perspective. *Am. Mineral.* 100 (10), 2026–2042.
- Steele-MacInnis, M., Esposito, R., Bodnar, R.J., 2011. Thermodynamic model for the effect of post-entrapment crystallization on the H_2O-CO_2 systematics of vapor-saturated, silicate melt inclusions. *J. Petrol.* 52 (12), 2461–2482.
- Su, Y., Huber, C., 2017. The effect of nonlinear decompression history on H_2O-CO_2 vesiculation in rhyolitic magmas. *J. Geophys. Res. Solid Earth* 122 (4), 2712–2723.
- Thoraval, C., Demouchy, S., 2014. Numerical models of ionic diffusion in one and three dimensions: application to dehydration of mantle olivine. *Phys. Chem. Miner.* 41 (9), 709–723.
- Toplis, M.J., 2005. The thermodynamics of iron and magnesium partitioning between olivine and liquid: criteria for assessing and predicting equilibrium in natural and experimental systems. *Contrib. Mineral. Petrol.* 149 (1), 22–39.
- Toramaru, A., 2006. BND (bubble number density) decompression rate meter for explosive volcanic eruptions. *J. Volcanol. Geotherm. Res.* 154 (3–4), 303–316.
- Venugopal, S., Moune, S., Williams-Jones, G., 2016. Investigating the subsurface connection beneath Cerro Negro volcano and the El Hoyo Complex, Nicaragua. *J. Volcanol. Geotherm. Res.* 325, 211–224.
- Walker, J.A., Carr, M.J., 1986. Compositional variations caused by phenocryst sorting at Cerro Negro volcano, Nicaragua. *Geol. Soc. Am. Bull.* 97 (9), 1156–1162.
- Wilson, L., Head, J.W., 1981. Ascent and eruption of basaltic magma on the Earth and Moon. *J. Geophys. Res.* 86 (NB4), 2971–3001.
- Witham, F., Blundy, J., Kohn, S.C., Lesne, P., Dixon, J., Churakov, S.V., Botcharnikov, R., 2012. SolEx: a model for mixed COHSCI-volatile solubilities and exsolved gas compositions in basalt. *Comput. Geosci.* 45, 87–97.
- Withers, A.C., Bureau, H., Raepsaet, C., Hirschmann, M.M., 2012. Calibration of infrared spectroscopy by elastic recoil detection analysis of H in synthetic olivine. *Chem. Geol.* 334, 92–98.
- Wunderman, R. e., 1995. Global Volcanism Program, 1995. Report on Cerro Negro (Nicaragua). Technical report. Bulletin of the Global Volcanism Network, 20:11. Smithsonian Institution.
- Zhang, Y., Ni, H., Chen, Y., 2010. Diffusion data in silicate melts. *Rev. Mineral. Geochem.* 72 (1), 311–408.

Supplement

August 8, 2019

1 Water diffusion model description

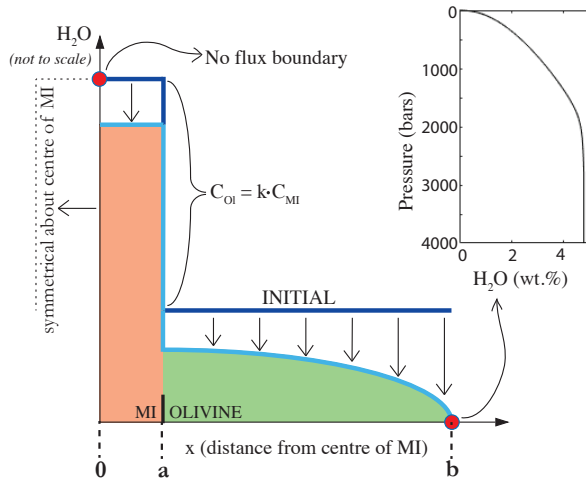


Figure S1: Model set-up for water loss from melt inclusions. Dark blue line shows initial water concentration from centre of MI to olivine edge. Over time, olivine and MI lose water to maintain equilibrium with degassing boundary condition (from Solex [Witham et al., 2012], P - H₂O trend shown inset). MI is assumed to remain in equilibrium with olivine, using a partition coefficient of 0.001 (measured in this study – see supplementary data table and Le Voyer et al. [2014], Hauri et al. [2006]).

To estimate the time during which H⁺ diffused out of each melt inclusion we solve the one-dimensional diffusion equation

$$\frac{\partial C}{\partial t} = \frac{\partial}{\partial x} \left(D \frac{\partial C}{\partial x} \right), \quad (1)$$

over the domain $0 \leq x \leq b$, where x is the spatial coordinate in the $\underline{\mathbf{a}}$ -direction from the center of the MI at $x = 0$ to the outer edge of the host olivine at $x = b$. Furthermore, t denotes time, C is H^+ concentration, and D is the piecewise continuous water diffusivity within the host olivine, and given by

$$D = D_{\text{MI}} \quad \text{at } 0 \leq x < a, \quad (2a)$$

$$D = D_{\text{OI}} \quad \text{at } a \leq x \leq b. \quad (2b)$$

Here, a is the radius of the melt inclusion, D_{MI} is the diffusivity of H^+ in the melt inclusion and D_{OI} is the diffusivity of H^+ in the olivine along $\underline{\mathbf{a}}$. The value of D_{OI} is temperature dependent and can be described by an Arrhenius equation, as determined in our experiments, and given by

$$D_{\text{OI}} = 9.6 \times 10^{-6} \exp \left(\frac{-125000}{8.314 \cdot T} \right) \quad (3)$$

Here we assume that D_{OI} is independent of the H^+ concentration in the olivine, due to the low concentrations (ppm level). Assuming, furthermore, isothermal conditions with $T = 1100 \text{ } ^\circ\text{C}$, D_{OI} is constant in all of our calculations, which leads to a value of value $D_{\text{OI}} = 10^{-9.76} \text{ m}^2/\text{s}$.

For each melt inclusion we solve Equation (1) using the MATLAB function `pdepe` over $0 \leq x \leq b$ with initial conditions

$$\begin{aligned} C &= C_0^{\text{MI}} && \text{at } t = 0 \text{ and } 0 \leq x < a, \\ C &= C_0^{\text{OI}} && \text{at } t = 0 \text{ and } 0 = x \leq b. \end{aligned} \quad (4)$$

Here C_0^{MI} is the initial melt inclusion H_2O concentration, while C_0^{OI} is the initial olivine H_2O concentration, related to C_0^{MI} by a partition coefficient of 0.001.

The boundary conditions are

$$\frac{\partial C}{\partial x} = 0 \quad \text{at } x = 0, \quad \text{and} \quad (5a)$$

$$C = C_b \quad \text{at } x = b. \quad (5b)$$

The Dirichlet boundary condition, C_b is the pressure dependent solubility of water in the melt at equilibrium. It is calculated using the Solex model (Witham et al., 2011). The pressure P is calculated at each time step as

$$P(t) = P_{\text{initial}} - dP/dt \cdot t \quad (6)$$

where dP/dt is given by

$$dP/dt = \frac{P_{\text{initial}} - P_{\text{final}}}{\tau} \quad (7)$$

where τ is the total ascent time.

The best fit total ascent time for each melt inclusion is determined using the MATLAB error minimization function, `fminbnd`, to minimize the error between the final melt inclusion H₂O concentration output from the model and that measured by SIMS.

2 Monte Carlo Simulations

We use Monte Carlo simulations in which H^+ diffusivity (D_{OI}) and olivine-melt partition coefficient (K_D) are allowed to vary independently. We run the simulation 10,000 times for each melt inclusion, each time drawing a different D_{OI} and K_D from a prior normal distribution. These distributions are shown in figure S2.

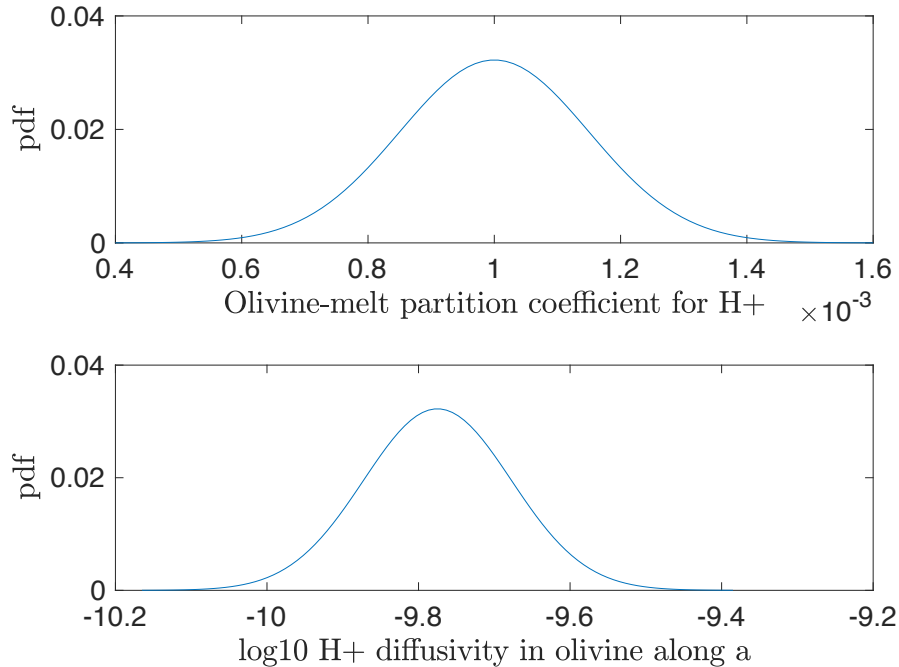


Figure S2: Prior normal distribution of $\log_{10}(D_{\text{OI}})$ and K_D . Distributions defined by $K_D = N(0.001, 0.0003/2)$ and $\log_{10}(D_{\text{OI}}) = N(-9.775, 0.1950/2)$, where $N(\text{mean}, \text{std})$ refers to a normal distribution.

The distribution for D_{OI} comes from a combination of uncertainty on the Arrhenius relationship from our dehydration experiments and temperature estimates from MI-olivine Mg thermometry. We calculate an upper and lower Arrhenius slope from the range in possible diffusivities (from fits to diffusion profiles) at 800 and 1000 °C. We extrapolate these slopes to 1100 °C ± 24 °C (2 standard deviation on temperature) to determine uncertainty in diffusivity for our models. The distribution for K_D comes from SIMS measurements of water in MIs and adjacent host olivine. The measured values range from 0.0008 to 0.0012, however, we believe these to be underestimates of the true partition coefficient since the olivine is measured at a finite distance from the MI - if we were able

to measure water in olivine right at the Ol-MI boundary it would be higher, so the inferred K_D would be higher. Therefore, we use a mean value for K_D of 0.001 and a 2σ value of 0.0003.

The Monte Carlo simulations show that uncertainty in $\log_{10}(dP/dt)$ is $\sim 10\%$ (see supplemental data table). Figure 2 shows several representative distributions of decompression rate for MIs from both eruptions.

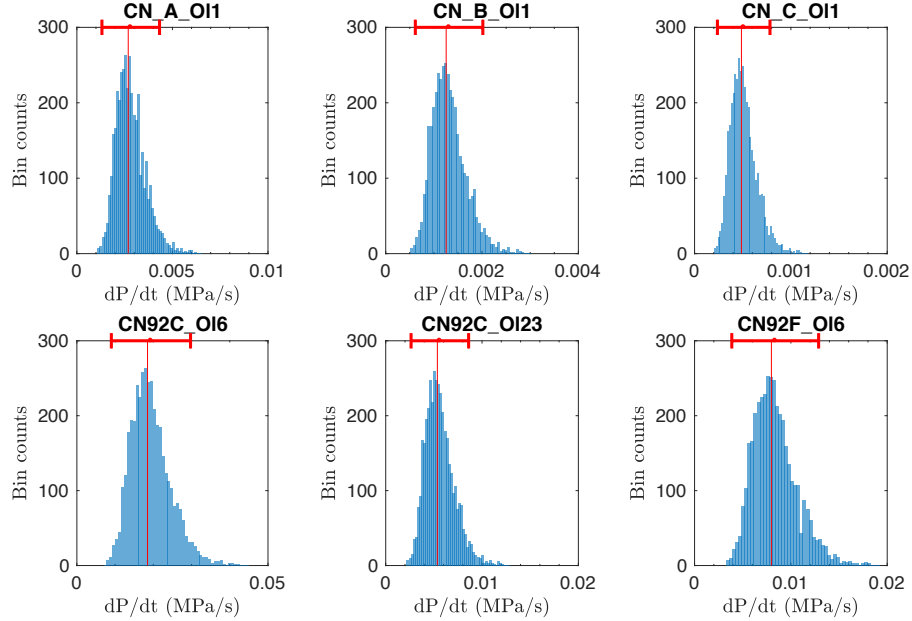
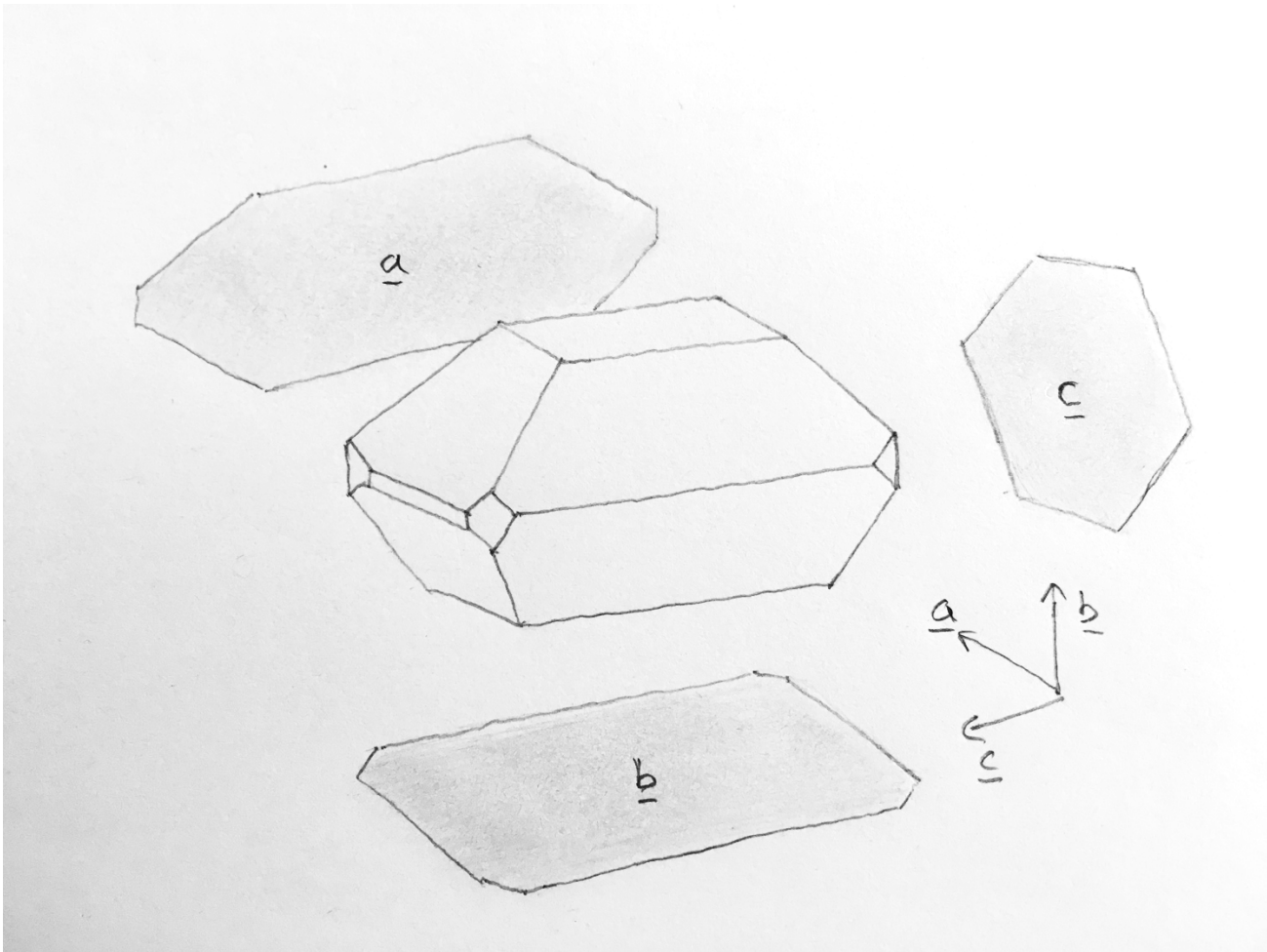


Figure S3: Posterior distribution of decompression rates for 10,000 Monte Carlo Simulations for 6 representative MIs. Upper 3 MIs from 1995, lower 3 from 1992. Red bar indicates 95% confidence interval.

3 Parameter Table

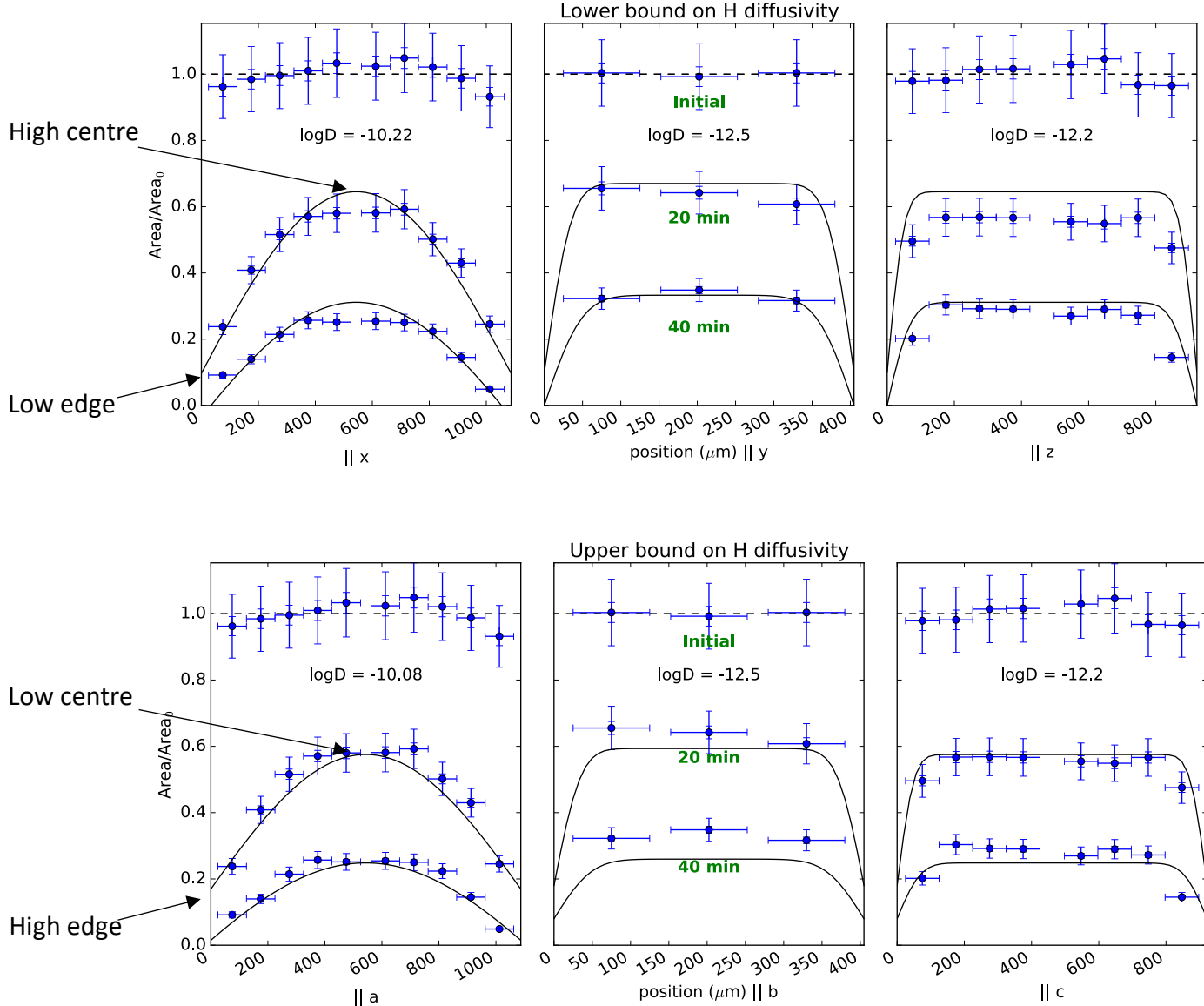
Symbol	Description	Value	Justification
D_{Ol}	H^+ diffusivity in olivine along $\underline{\mathbf{a}}$ ($\text{m}^2/\text{2}$)	$10^{-9.76}$	Arrhenius relationship from dehydration experiments (this study)
$\delta\rho$	Olivine density/melt density	1.2	Chen et al. [2013]
T	Temperature ($^\circ\text{C}$)	1100	Mg-melt thermometry on MIs in this study (eq. 4 in Putirka et al. [2007])
K_D	Melt-olivine partition coefficient	0.001	Hauri et al. [2006], Le Voyer et al. [2014]
P_{final}	Final pressure (MPa)	0.3	Value of Solex degassing boundary condition for matrix glass H_2O concentration of 0.1 wt.% (measured by SIMS)
MI-specific parameters			
P_{initial}	Initial pressure (MPa)		Value of Solex degassing boundary condition for restored MI H_2O concentration (measured by SIMS)
C_0^{MI}	Initial MI H_2O (wt.%)		From K_2O systematics, this study, section 5.2.2
C_f^{MI}	Final MI H_2O (wt.%)		SIMS measurement
a	MI radius (m)		Optical measurement, average of long and short MI axes
b	Distance between MI centre and Ol edge along $\underline{\mathbf{a}}$ (m)		Optical measurement
D_{melt}	H^+ diffusivity in melt ($\text{m}^2/\text{2}$)		Eq. 22 in Zhang and Ni [2010], using $\frac{1}{2} \left(C_0^{\text{MI}} + C_f^{\text{MI}} \right)$ for C_w

4. Olivine morphology



Letters on planes refer to the name of that plane: plane **a** has directions **b** and **c** within it etc.

5. Upper and lower bounds on whole block profile fitting



The profiles do not trend towards zero at the crystal edge, and this gives rise to some uncertainty in diffusivity arising from the choice in edge concentration. Upper and lower bounds on edge concentration were chosen to be as high or low as possible while still allowing the profiles to be fit within the error bars. The upper bound on the edge concentration requires a faster diffusivity in order to fit the profile, while the lower bound on the edge concentration requires a slower diffusivity.

6. Estimating initial H⁺ concentration

The total absorbance of an anisotropic material is given by Libowitzky and Rossman, 1996 as:

$$E_{tot} = E_a + E_b + E_c$$

For CN-block1, we have measurements on face B with E||a, and unpolarised measurements on face A, which will be a combination of E||b and E||c.

We estimate total absorbance as $E_a + 2 \cdot E_{unpol}$

This gives us an initial water concentration of ~ 9 ppm using the Bell calibration.

For CN-block2, we only have measurements with E||b and E||c on face A, with no measurements with E||a. Since most of the absorbance signal is measured with E||a, this presents a problem for estimating total water.

We calculate the ratio of absorbance area with E||a to that with E unpolarised in CN-block1, and use this ratio to infer the ‘missing’ E||a signal in CN-block2:

CN-block1:

$$\text{total: bc ratio} = \frac{\text{area}_{E||a} * (2 \cdot \text{area}_{unpol})}{2 \cdot \text{area}_{unpol}} = 2.46$$

CN-block2:

$$E_{tot} = (E_a + E_b) * \text{total: bc ratio}$$

which gives us an initial water concentration of ~ 5 ppm using the Bell calibration.

7. Saturation Pressures

Saturation pressures from VolatileCalc using MI H₂O-CO₂. T = 1100°C, SiO₂ = 49 wt.%, closed system degassing, initial (restored) water.

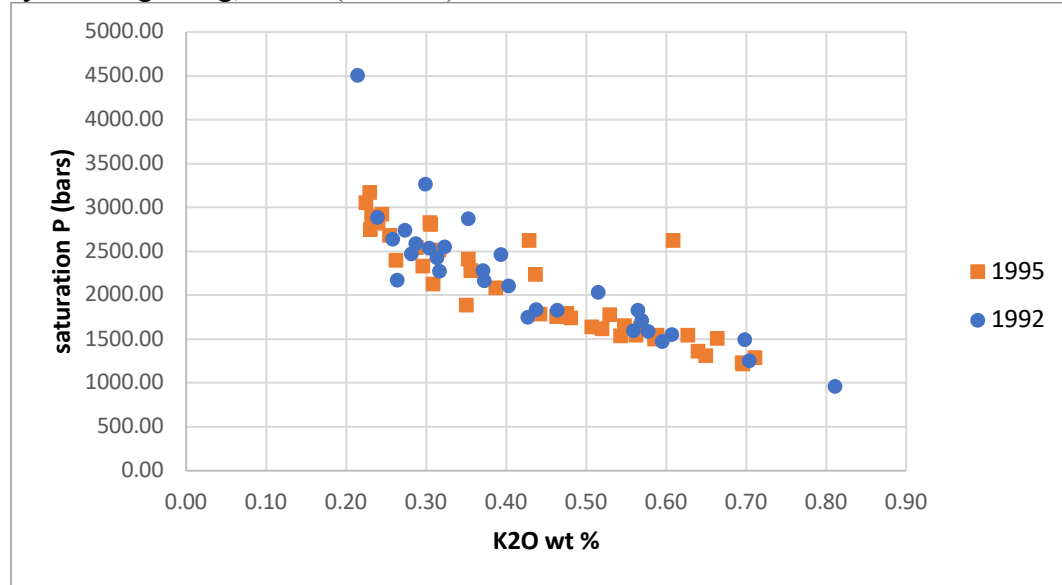
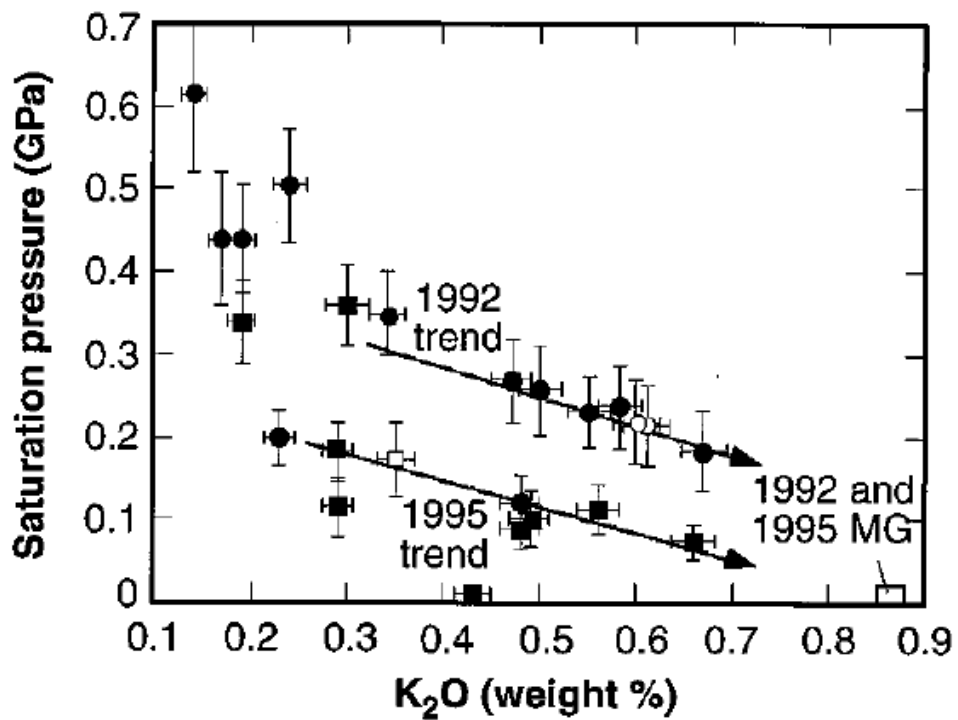


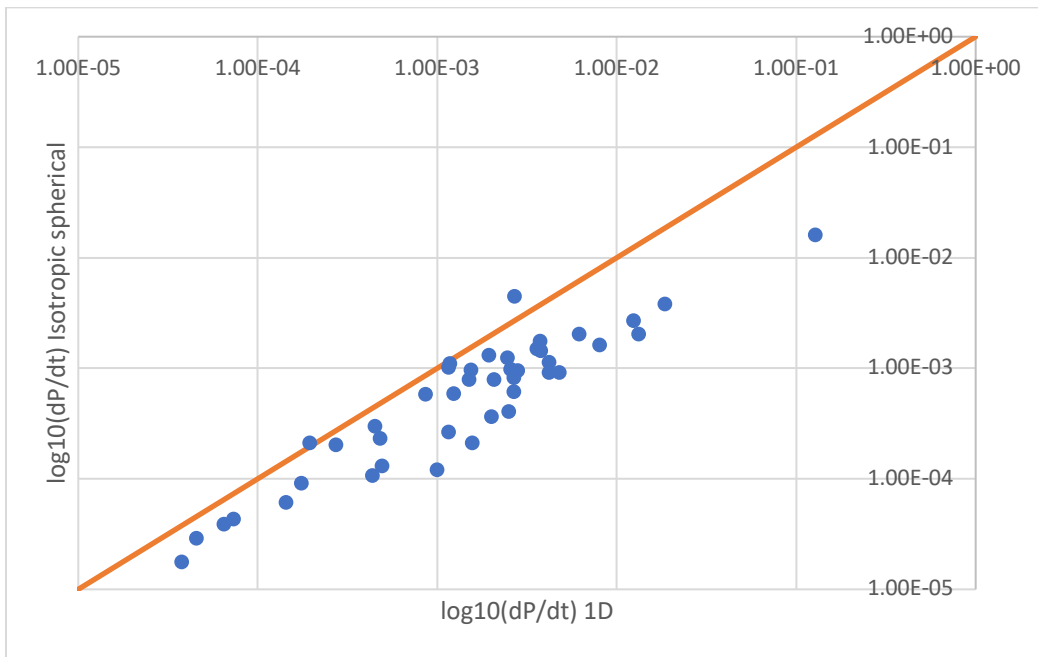
Fig. 3 in Roggensack et al., 1997:



8. Isotropic spherical model

Comparison of decompression rate results for 1D oriented (x axis) and isotropic spherical model (y axis). Isotropic model uses a diffusivity corresponding to unoriented olivine dehydration experiments with $D = 10^{-11.47} \text{ m}^2/\text{s}$ (grey field in Arrhenius plot) and taking the MI to olivine edge distance as the shortest distance, regardless of orientation.

The isotropic spherical model consistently under-predicts the decompression rate on average by a factor of 3, and up to a factor of 8 for individual samples. The offset is likely due to high uncertainties in diffusivity from the experiments of Chen et al., 2011 and inaccuracies in using an isotropic diffusivity for an anisotropic problem.



References

- Yang Chen, Ariel Provost, Pierre Schiano, and Nicolas Cluzel. The rate of water loss from olivine-hosted melt inclusions. *Contributions to Mineralogy and Petrology*, 162(3):625–636, 2011. ISSN 00107999. doi: 10.1007/s00410-011-0616-5.
- Yang Chen, Ariel Provost, Pierre Schiano, and Nicolas Cluzel. Magma ascent rate and initial water concentration inferred from diffusive water loss from olivine-hosted melt inclusions. *Contributions to Mineralogy and Petrology*, 165(3):525–541, 2013. ISSN 00107999. doi: 10.1007/s00410-012-0821-x.
- Erik H. Hauri, Glenn A. Gaetani, and Trevor H. Green. Partitioning of water during melting of the Earth’s upper mantle at H₂O-undersaturated conditions. *Earth and Planetary Science Letters*, 248(3-4):715–734, aug 2006. ISSN 0012-821X. doi: 10.1016/J.EPSL.2006.06.014. URL <https://www.sciencedirect.com/science/article/pii/S0012821X06004304>.
- Marion Le Voyer, Paul D. Asimow, Jed L. Mosenfelder, Yunbin Guan, Paulj Wallace, Pierre Schiano, Edward M. Stolper, and John M. Eiler. Zonation of H₂O and F concentrations around melt inclusions in olivines. *Journal of Petrology*, 55(4):685–707, 2014. ISSN 14602415. doi: 10.1093/petrology/egu003.
- Eugen Libowitzky and George R Rossman. Principles of quantitative absorbance measurements in anisotropic crystals. *Physics and Chemistry of Minerals*, 23 (6):319–327, 1996. ISSN 0342-1791.
- Keith D. Putirka, Michael Perfit, F. J. Ryerson, and Matthew G. Jackson. Ambient and excess mantle temperatures, olivine thermometry, and active vs. passive upwelling. *Chemical Geology*, 241(3-4):177–206, 2007. ISSN 00092541. doi: 10.1016/j.chemgeo.2007.01.014.
- Kurt Roggensack, Richard L Hervig, Steven B McKnight, N Stanley, and Stanley N Williams. Explosive Basaltic Volcanism from Cerro Negro Volcano : Influence of Volatiles on Eruptive Style. *Science*, 277(5332):1639–1642, 1997. ISSN 00368075. doi: 10.1126/science.277.5332.1639.
- Fred Witham, Jonathan Blundy, Simon C. Kohn, Priscille Lesne, Jacqueline Dixon, Sergey V. Churakov, and Roman Botcharnikov. SolEx: A model for mixed COHS_nCl-volatile solubilities and exsolved gas compositions in basalt. *Computers and Geosciences*, 45:87–97, 2012. ISSN 00983004. doi: 10.1016/j.cageo.2011.09.021.
- Y. Zhang and H. Ni. Diffusion of H, C, and O Components in Silicate Melts. *Reviews in Mineralogy and Geochemistry*, 72(1):171–225, 2010. ISSN 1529-6466. doi: 10.2138/rmg.2010.72.5.